Zeitschrift: Helvetica Physica Acta
Band: 66 (1993)
Heft: 7-8

Vereinsnachrichten: Rapport de la réunion d'automne de la SSP
Autor: [s.n.]

Helv Phys Acta
Vol. 66 (1993)

0018-0238/93/080877-32$1.50+0.20/0

SURFACE MORPHOLOGY AND ROUGHNESS OF TiO_2 THIN FILMS INVESTIGATED WITH SCANNING FORCE MICROSCOPY

W. GUTMANNSBAUER, H. HAEFKE, M. RÜETSCHI, H.-J. GÜNTHERODT, J. STAUB† and K. BANGE††

Institut für Physik, Universität Basel, Klingelberstr. 82, CH-4056 Basel, Switzerland
†Institut für Angewandte Physik, Technische Hochschule Darmstadt, Germany
††Schott Glaswerke, Forschung und Entwicklung, Mainz, Germany

The morphology and roughness of TiO_2 thin films on glass substrates were studied with scanning force microscopy. The quality of the film surface, expressed as rms values, depends on the deposition method used and on the evaporation parameters.

Thin-film coatings (e.g., TiO_2) are applied to effect a desired change in chemical and/or physical properties of glass surfaces. A great number of optical thin film components increase or decrease light intensity, split light beams or act as light guides. The optical properties of such films are strongly affected by the surface roughness.
In this study, we have investigated the surface morphology of TiO_2 thin films produced by various reactive deposition methods: 1) Ion beam sputtering (IBS), 2) ion plating (IP) and 3) electron beam evaporation (RE). In order to prepare TiO_2 films, titanium was sputtered or evaporated in a reactive oxygen atmosphere. Polished silica glasses, exhibiting surface roughness ranging from about 1 to 2 nm, were used as substrates. The TiO_2 films were deposited at substrate temperatures in the range of 70 - 260 °C and with film thicknesses varying from 160 to 640 nm. The film surfaces were studied with the scanning force microscope (SFM) operated in the repulsive contact mode at room temperature. Figure 1 shows force micrographs of 480 nm thick TiO_2 thin films grown by IBS (fig. 1a), IP (fig. 1b) and RE (fig. 1c), respectively. Films produced by IBS and IP exhibit an amorphous structure, whereas RE-films are polycrystalline with anatase structure [1, 2]. On the surface of the latter, no significant features are detectable with the force microscope (fig. 1c). Contrary to this, the surface of the IBS- and IP-films are covered by holes; their coverage of the surface is 2% and 25%, respectively. At higher magnification, the force microscope reveals that the surfaces of these holes are characterised by small grains. In the hole-free regions of the TiO_2 films, however, no grain structure could be imaged with the SFM. Using cross-section preparation for transmission electron microscopy examination, the crystalline grains were identified as the rutile modification of TiO_2 [3]. A possible explanation for the formation of the rutile phase might be the compressive stress, arising from the bombardment of the growing film by atoms and ions. The kinetic energy of the arriving particles (10 - 100 eV) causes the atoms to be incorporated into spaces of the growing film that are smaller than the usual atomic volume [4]. In order to reduce this stress, the IBS- and IP-films change to a denser state and form finally the rutile phase at the surface region. Although the number of holes increases with increasing film thickness, the rms values are rather constant. Moreover, the rms values of the IBS- and IP-films are in the same range as those of the RE-films (cf. fig. 2). TiO_2 films deposited by IP exhibit similar surface properties as the IBS-films. The smallest rms value was determined to be 0.7 nm for 160 nm thick IP-films. At larger film thicknesses the number of holes and the rms values increase and reach a maximum at 480 nm (figs. 1 and 2). Because the temperature of the substrate is steadily increasing in this deposition method, the amorphous particles around the holes crystallise to form anatase. We assume that this could remove some of the stress from the film. This would explain the decrease of the rms values at a film thickness of 640 nm (Fig. 2). Figure 3 shows rms values of IBS-, IP- and RE-films (d = 480 nm) compared with rms values of IBS- and IP-films (IBS*, IP*) measured without surface defects. We conclude that if one could find a way to

thin films without the formation of rutile, the preparation of TiO_2 coatings with very low rms values would be possible.

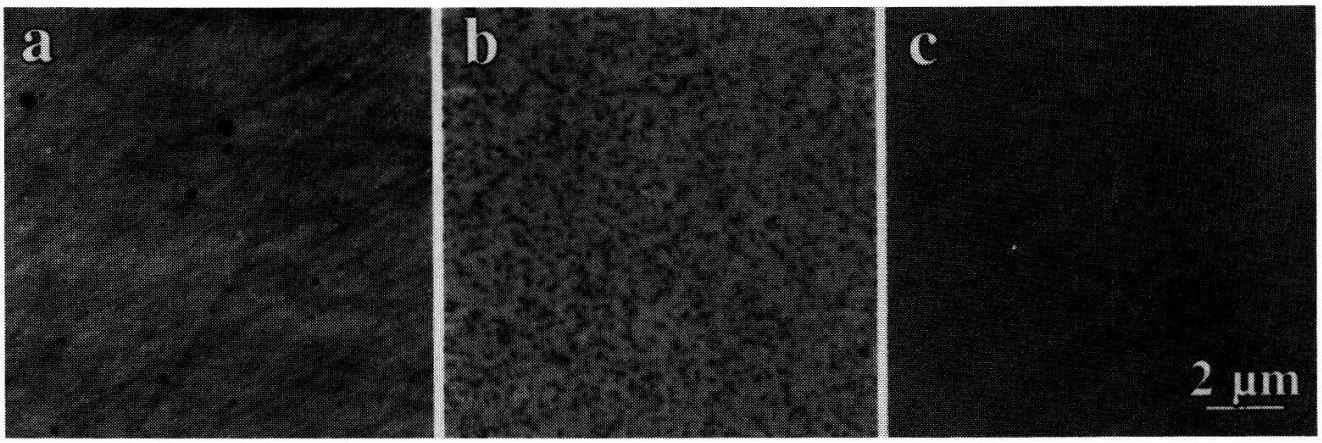

Figure 1: Force micrographs of TiO_2 thin films deposited by various methods: (a) IBS, (b) IP and (c) RE. The nominal film thickness is 480 nm.

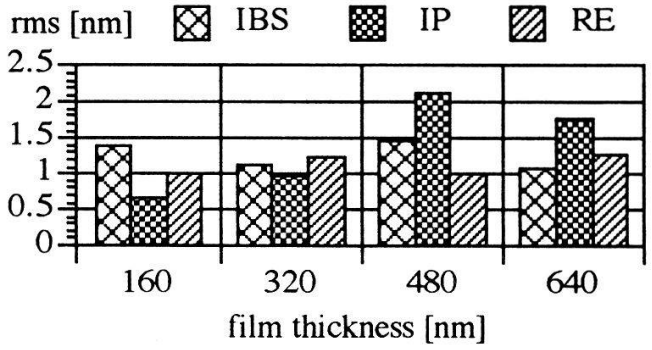

Figure 2: Diagram of rms values as a function of the thickness of TiO_2 thin films produced by various methods.

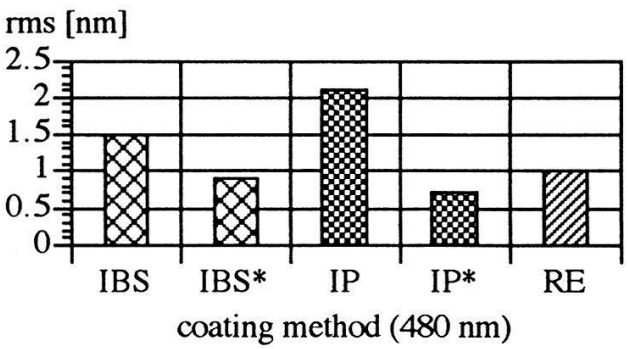

Figure 3: Diagram of rms values of IBS-, IP- and RE-films (d = 480 nm) compared to rms values of hole-free surface areas in IBS- and IP-films (IBS*, IP*).

References

[1] E. Meyer, H. Haefke, H.-J. Güntherodt, O. Anderson, K. Bange, Glastech. Ber. 66, 2 (1993).

[2] J. Staub, Thesis, Darmstadt (1993).

[3] K. Bange et al., in preparation.

[4] C. A. Davis, Thin Solid Films 226, 30 (1993).

Resonant inverse photoemission of cerium valence fluctuators

P. Weibel, M. Grioni, D. Malterre, B. Dardel and Y. Baer
Institut de Physique, Université de Neuchâtel, CH-2000 Neuchâtel Switzerland

We present the first results of a Resonant Inverse Photoemission investigation of mixed-valent cerium compounds. A two-orders-of-magnitude enhancement of the spectral intensity is observed when the excitation energy crosses the Ce M_5 ($3d_{5/2} \rightarrow 4f$) absorption edge. The complex lineshape of the resonance reflects the hybrid character of the ground state, and is qualitatively interpreted in the framework of the Anderson impurity model. Resonant Inverse photoemission appears as a new and powerful probe of the electronic structure of strongly correlated materials.

Photoemission (PES) and inverse photoemission (IPES) spectroscopies provide unique and complementary information on the electronic structure of strongly correlated solids, like the mixed-valent Ce and Yb-based materials. In these systems, fundamental considerations require that the combined PES/IPES *4f* spectra be interpreted as the many-body spectral function of the Anderson impurity Hamiltonian. In practice, a quantitative analysis must face the difficulty of extracting the *4f* contribution from the measured spectra. For the occupied part of the spectral function this problem is, to some extent, solved by the well-established resonant PES (RESPES) that exploits resonances in the *4f* photoionization cross section. No similar solutions have been developed so far for IPES, which is also plagued by low intensity levels. On the other hand some early experimental evidence [1] indicates that the *4f* IPES cross section also exhibits resonances (namely at the $3d \rightarrow 4f$ absorption edges), and suggest the possibility of extending the typical advantages of RESPES to the investigation of the unoccupied states.

The first results of a new, dedicated IPES spectrometer operating at excitation energies around to the Ce M_5 edge (883 eV), confirm these expectations and demonstrate the potentialities of resonant IPES (RIPES). Figure 1 shows an example of resonant enhancement of the IPES spectral function in $CeNi_2$, a material characterized by a rather strong *4f* configuration mixing in the ground state. Off-resonance (e.g. at V_c=877 V), the measured intensity is comparable to that of traditional X-ray IPES, but a dramatic hundredfold intensity increase is observed around 880 V. The amplification is the consequence of the quantum interference between the usual IPES deexcitation channel, and indirect channels involving the excited $3d^94f^2$ and $3d^94f^3$ configurations of the Ce impurity. The characteristic features of the Ce IPES spectrum, that correspond to final states of predominantly f^1 (near the high photon energy limit) and f^2 (4-5 eV below) character, are both enhanced. This is evident from Fig. 2, where the energy dependence of their integrated intensities (Constant Final State curves, CFS) is displayed. The separation (~2 eV) of the two resonances reflects the different energies of the intermediate excited states, while their width is essentially determined by

selection rules that severely limit the possible transitions within the intermediate and final state manyfolds [2].

Analogous measurements have been performed on various Ce systems characterized by different hybridization strengths between the Ce *4f* and the conduction band states. We have observed that the intensity ratio of the "f^1" and "f^2" resonance lines is strongly material-dependent, and reflects the degree of configuration mixing in the ground state. RIPES offers therefore entirely new possibilities for the spectroscopic investigation of valence fluctuators.

The possible application of RIPES, however, are not limited to this specific subject. RIPES presents, similarly to RESPES, an intrinsic site and symmetry selectivity. These properties, together with the demonstrated intensity enhancement, should quite generally be extremely valuable in studies of materials with (partially) localized electronic states. Extensions of the technique to uranium systems, and to specific surface and interface problems are presently under way.

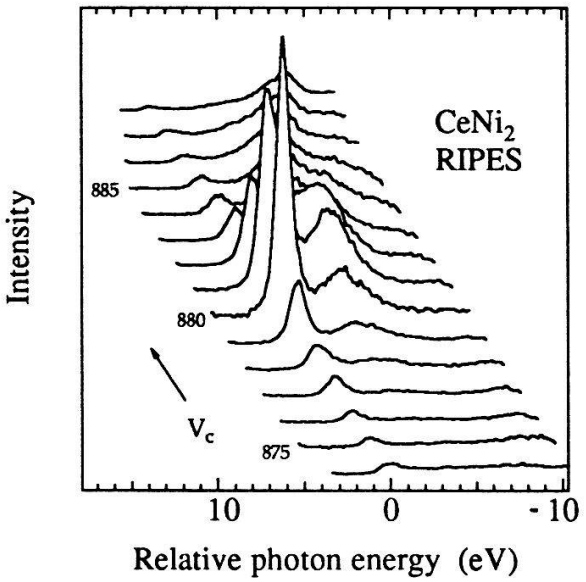

Fig. 1: IPES spectra collected at various excitation energies through the Ce M_5 absorption edge. The spectra are labelled by the accelerating voltage V_c of the primary electron beam.

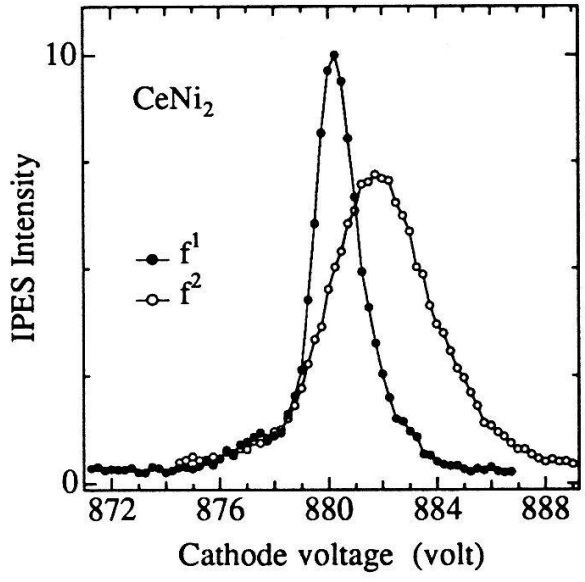

Fig. 2: CFS curves obtained by integrating, as a fonction of excitation energy, the RIPES signal within two energy windows that follow the positions of the f^1 and f^2 peaks.

References

[1] R.J. Liefeld, A.F. Burr and M.B. Chamberlain, Phys. Rev. A **9**, 316 (1974).

[2] P. Weibel, M. Grioni, D. Malterre, B. Dardel and Y. Baer, submitted.

TIME DEPENDENCE OF FLUX PENETRATION INTO $Y_1Ba_2Cu_3O_7$ TUBES

H. Castro, E. Holguin and L. Rinderer
Institut de Physique Expérimentale, Université de Lausanne, CH-1015 Lausanne, Switzerland

When we switch on an external magnetic field parallel to the axis of a HTSC cylinder, the flux penetrates in a way that can be explained by the flux-flow theory as previously reported by our group. Here we present the predicted time dependence for the shielding current, field-front penetration speed and trapped field for an $Y_1Ba_2Cu_3O_7$ cylinder stabilized with 5% Ag. Interesting conclusions concerning the characterization and practical applications of this material to such devices as magnetic shields, current limiters, etc. can be drawn.

The study of vortex dynamics in HTSC ceramics is a very interesting problem though a complex one. The granular structure composed by strong superconducting grains known as the Abrikosov medium interconnected by a weak link network called the Josephson medium, behave in an intricate way. Nonetheless, the work done during the last years helps to clarify the role played by each of these mediums in the response to a magnetic field. It is accepted [1] that at sufficiently low fields the flux lines penetrate the material threading the Josephson medium so avoiding the highly diamagnetic grains. At higher fields they start penetrating the grains originating new features in the vortex dynamics. Some phenomenological models derived from the Kim-Anderson and from the Bean's one have been successfully applied to explain certain aspects in the magnetic behavior of these materials for a DC and for a sinusoidal excitation.

Another approach to analyze the dynamics of this system is to study the response to a square shaped magnetic field pulse, as proposed by Holguin [2]. we apply this type of excitation parallel to the axis of a tubular HTSC sample, then measure the speed of flux penetration by means of a pick up coil located in the bore. This experiment permits the direct observation of the basic characteristics of the flux penetration phenomenon and particularly the study of the transient behavior of the system before the steady 'critical state' settles down. The proposed theory [3], based on flux flow and Bean's model satisfactorily explains our experimental data [4].

In this paper we present the corresponding theoretical prediction for the time dependence of the shielding current $J_J(t)$, wave front speed of penetration $v(t)$, trapped field in the bore $H_i(t)$ and the dissipated power in the sample $P(t)$; for an $(Y_1Ba_2Cu_3O_7)_{0.95}$ $Ag_{0.05}$ cylinder at 77K for small field amplitudes such that the grains remain in the meissner state (i.e. $H_e < H_{c1g}$).

The basic equations from which we obtain the time dependence of the concerning variables are eq. 14 in ref. 3 for $t > \Delta t$ and the exact solution to eq. 8 in the same reference, which relates the shielding current to time for $t \leq \Delta t$,

$$t = \left(\frac{\mu w^2 H_{c2J}}{2\rho_{nJ} H^*} \right) \cdot h \cdot \left\{ \ln\left(\frac{j}{j-1} \right) - \frac{1}{j} \right\} \qquad (1)$$

where $j = J_J(t) / J_{cJ}$ and $h = H_e / H^*$ is the normalized applied field. J_{cJ} is the critical current as in Bean's model, w the wall thickness of the sample, μ is the magnetic permeability $\mu = \mu_o \cdot \mu_{eff}$, with μ_{eff} as defined in ref. [1], H_{c2J} and ρ_{nJ} are the second critical field and the resistivity of the Josephson medium, respectively. H^* is the threshold field below which no flux can reach the hole of the sample (shielding field).

The behavior of the shielding current is shown in fig. 1 (left scale). J_J diverges for $t \to 0$ as a consequence of the assumption of an ideal step like applied field. In the limit when $t \to \infty$ we obtain the Bean critical state $J_J(t) \to J_{cJ}$.

In the same figure (right scale) we have the field arriving to the hole. This trapped field is given by the equation $H_i(t) = H_e - J_J(t) \cdot w$ and can be fitted by a function of the type

$$H_i(t) = H_e \cdot \left\{1 - \exp\left[-(t - \Delta t)/\tau\right]\right\} - H^* \qquad (2)$$

Here we introduced two field-dependent parameters [5] characterizing this phenomenon. The penetration time, Δt and the time constant τ which defines the exponential increase of the flux in the hole. For the applied field $H_e = 2 \cdot H^*$ we have $\Delta t = 0.77$ μs and $\tau = 2$ μs.

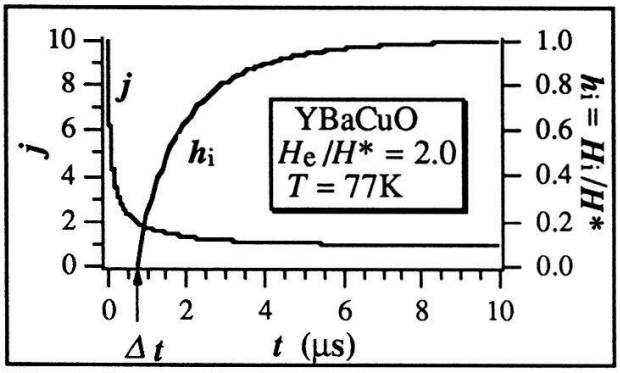

Fig. 1 Normalized shielding current and trapped field vs. time

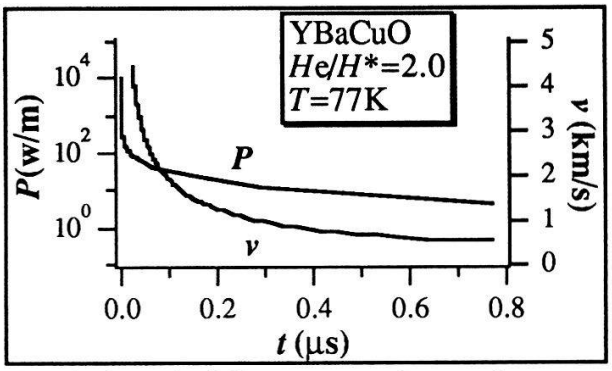

Fig. 2 Speed of flux penetration and dissipated power vs. time

In fig. 2 we have the electrical power dissipated per unit length in the sample (left scale). This is, in fact, the work done by the penetrating field against the viscous force, as expected from the flux flow theory. The curve was computed by integrating in the sample's volume the expression

$$p(t) = \rho_{nJ} \frac{H(r,t)}{H_{c2J}} \left[J_J(t) - J_{cJ}\right]^2 \qquad (3)$$

which can be used to compute the overheating of the sample during this process.
The speed of flux penetration, also shown in fig. 2 (right scale) is given by the equation

$$v(t) = w \cdot \frac{h}{j^2} \cdot \frac{dj}{dt} \qquad (4)$$

These results show how a fast changing magnetic field induces high shielding currents which decay rapidly to the steady 'critical state' with characteristic times dependent on the amplitude of the applied field. This theory allows to know the time development of the main variables, as the penetration time, decay time constant, speed of field penetration and the power dissipated in the sample. From the practical point of view our results can be used to evaluate the performance of these materials as magnetic shields in the case of pulsed or high frequency fields. Another interesting case is the current limiter for which we need to know the penetration time and the overheating of the sample for a sudden increase of the transport current.

We thank Drs. D. Abukay and V. Soares for fruitful discussions.
This work was partially supported by the Swiss National Science Foundation.

References

[1] J. R. Clem, Physica C 153-155 (1988) 50.
[2] E. Holguin, J. F. Loude and H. Berger, *Physica* C 197 (1992) 167.
[3] G. Ravikumar, *Solid State Commun.* **77** (1991) 447.
[4] H. Castro et al., *Helv. Phys. Acta* **66** (1993) 67.
[5] H. Castro et al., presented at *LT20 conference*, Eugene, Oregon (1993).

Single crystal substrates for thin film growth of HT_cSC studied by scanning force microscopy

R. Sum, R. Lüthi, H.P. Lang, and H.-J. Güntherodt

Institute of Physics, University of Basel, Klingelbergstr. 82, CH-4056 Basel, Switzerland

We applied scanning force microscopy to study the surface morphology of single crystalline substrates used for thin film growth of high temperature superconductors. By annealing the substrates ($SrTiO_3$, $LaAlO_3$, $NdGaO_3$ and MgO) at 800 °C in 1 atm of oxygen it was possible to improve its surface conditions.

Single crystalline substrates being commonly used as substrates for the deposition of high temperature superconductors (HTSC) are usually cut and polished mechanically. Due to this manufacturing process residual materials like polishing compounds and other surface contaminations have to be removed before deposition of the HTSC thin film. Generally, the substrates are rinsed in acetone or methanol and annealed in an oxygen atmosphere prior to the deposition of HTSC thin film [1,2]. We used scanning force microscopy (SFM) to investigate the effects of these cleaning methods and compared the cleaned samples to the same ones without any treatment.

SFM has been carried out in air at room temperature using silicon cantilevers. Images were taken in the constant force mode applying forces of about 10 nN.

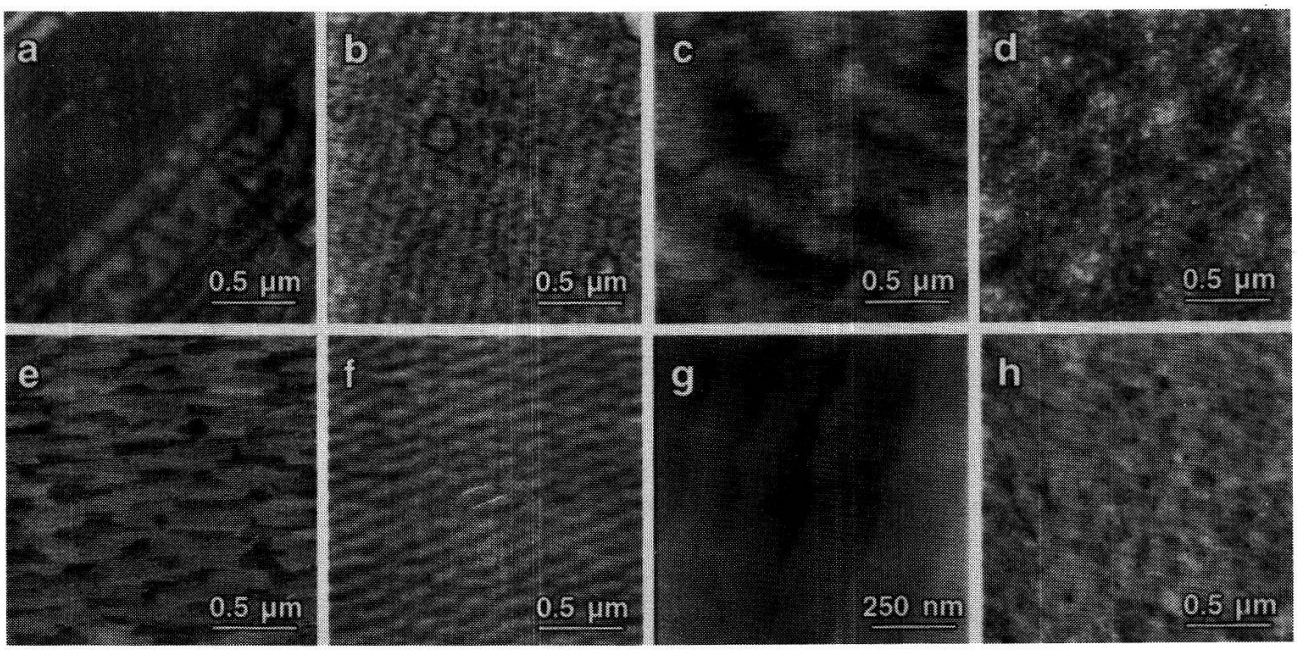

Figure 1: SFM images of single crystals (as received): (a) $SrTiO_3$, (b) $LaAlO_3$, (c) $NdGaO_3$, (d) MgO; annealed at 800 °C in O_2: (e) $SrTiO_3$, (f) $LaAlO_3$, (g) $NdGaO_3$, (h) MgO.

Figure 1 shows the (100) surfaces of (a) $SrTiO_3$, (b) $LaAlO_3$, (c) $NdGaO_3$ and (d) MgO single crystalline substrates as received from the suppliers.

PV/RMS	$SrTiO_3$	$LaAlO_3$	$NdGaO_3$	MgO
as received	25 nm/4.1 nm	10 nm/1.6 nm	1.5 nm/0.3 nm	2.5 nm/0.5 nm
annealed in O_2	6 nm/4.5 nm	30 nm/4.2 nm	4 nm/0.6 nm	20 nm/4.0 nm

Table 1: Roughness values (Peak to Valley (PV) and RMS) obtained from the samples in fig. 1.

The surface roughness values were determined by SFM and are compiled in table 1. Annealing the substrates at 800 °C in 1 atm of oxygen provides better conditions for imaging the sample with the SFM but increases its roughness (see table 1). In fig. 1 steps are visible: (e) on $SrTiO_3$, (f) on $LaAlO_3$ (several unit-cells in height) and (g) on $NdGaO_3$ (one unit-cell in height). However, MgO shows no distinct step structure.

The surface of the untreated $SrTiO_3$ substrates is covered by a layer of surface contamination. We observed that this layer can be easily wiped away by just scanning over an area several times. Figure 2a shows such a contaminated $SrTiO_3$ surface before zooming in the area in question. Figure 2b is an image of the same area after having scanned a smaller part of it (marked by a dashed square in fig. 2a) 5 times. From the image it becomes obvious that part of the contaminating material has been removed and wiped to the left and to the right border of the modified area.

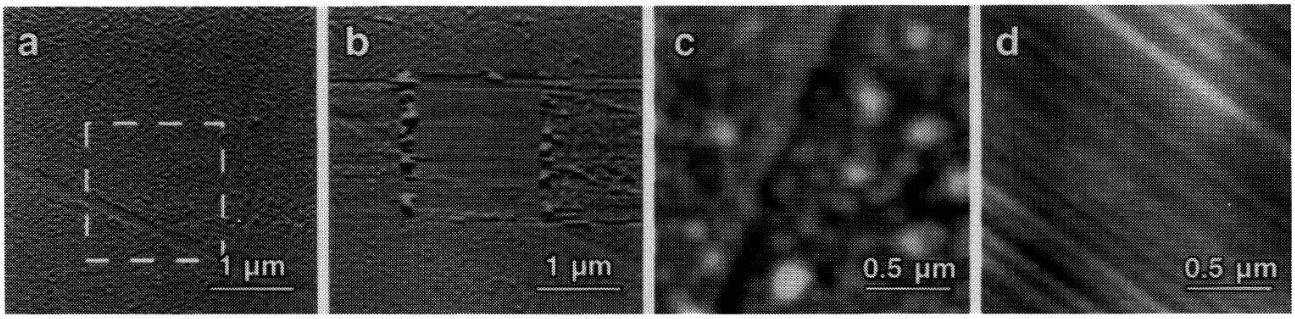

Figure 2: (a) Contamination layer on $SrTiO_3$, (b) modification after having scanned a smaller area 5 times, (c) cleaved MgO single crystal stored in air for 2 months, (d) freshly cleaved MgO single crystal.

It is well known that MgO reacts with the ambient air forming hydroxides and carbonates deteriorating the growth conditions for HTSC material [3,4].

Figure 2c shows the surface of a cleaved MgO single crystal having been stored in the ambient for 2 months. The surface is covered by particles of up to 0.5 μm in size. A MgO single crystal surface cleaved immediately before imaging by SFM (fig. 2d) exhibits no particles. Only the typical steps due to cleaving the crystal are present.

REFERENCES

[1] C. B. Eom, J. Z. Sun, B. M. Lairson, S. K. Streiffer, A. F. Marshall, K. Yamamoto, S. M. Anlage, J. C. Bravman and T. H. Geballe, Physica C **171**, 354 (1990).

[2] J. Burger, Ph. D. Thesis, Erlangen 1992.

[3] D. Hesse and H. Bethge, J. Cryst. Growth **52**, 875 (1981), D. Hesse and H. Bethge, *ibid.* **65**, 69 (1983).

[4] H. Haefke, H. P. Lang, R. Sum, H.-J. Güntherodt, L. Berthold, and D. Hesse, Appl. Phys. Lett. **61**, 2359 (1992).

Low Temperature Annealing of Ion-implanted KNbO3 Waveguides

T. Pliska, D.H. Jundt, D. Fluck and P. Günter

Nonlinear Optics Laboratory, Institute of Quantum Electronics, Swiss Federal Institute of Technology, ETH Hönggerberg, CH-8093 Zürich, Switzerland

M. Fleuster and Ch. Buchal

Institut für Schicht- und Ionentechnik, Forschungszentrum Jülich (KFA), D-52425 Jülich

We report results on annealing of ion-implanted channel waveguides in $KNbO_3$. The samples were heated up to 150°C and kept at this temperature for several hours. The waveguide transmission was measured in situ and after the annealing process. The loss coefficient was typically reduced by 1.0cm^{-1} at 454nm, 0.5cm^{-1} at 633nm and 0.2cm^{-1} at 860nm after an annealing time of 7 hours resulting in total waveguide loss coefficients of 1.8cm^{-1}, 0.7cm^{-1} and 1.3cm^{-1}, respectively.

The use of waveguides for nonlinear optical interactions is very attractive due to the tight beam confinement over long interaction distances. $KNbO_3$ was shown to be particularly suitable for second harmonic generation (SHG) into the blue and green spectral range thanks to its large nonlinear optical susceptibilities, its room-temperture phasematchibility at 860nm, its transparency down to 390nm and its very high threshold to optical damage [1], [2].
Ion implantation and sputter deposition are the only methods reported so far to produce waveguides in $KNbO_3$ [3], [4]. The $KNbO_3$ waveguides used in this work were formed by low-dose irradiation of a $KNbO_3$ substrate with MeV He^+ ions. By this technique low-loss planar and channel waveguides were produced [5], [6]. Recently we reported results on SHG in ion implanted $KNbO_3$ waveguides [7], [8].
In this letter we report results on post-implantaion annealing of $KNbO_3$ channel waveguides. The waveguide losses were considerably reduced by a low-temperature annealing process and the conversion efficiency for Cerenkov-type SHG was increased by a factor of two.
Irradiation of a solid with high energy ions causes electronic and nuclear damage. Ions penetrating into the solid will undergo inelastic scattering with bound electrons of the atoms of the solid. Thus the ions loose energy by electronic excitation or ionisation. This leads to the formation of colour centers. As the ions slow down nuclear collisions become dominating. Nuclear damage results in lattice distortions and partial amorphisation leading to the formation of a barrier layer with decreased refractive index. In this way a waveguiding structure is formed where electronic damage dominates in the waveguiding region whereas nuclear damage prevails in the index barrier.
The colour centers formed by electronic damage cause absorption in the visible spectral range. Therefore it is crucial to keep electronic damage as low as possible. However the higher the implantation dose is the lower the leakage of light through the index barrier. Thus electronic damage cannot be avoided completely during the implantation process and has to be diminshed by an anneling technique after the implantation.
In our measurement we observed the change of the waveguide losses in dependence of the annealing time. For the annealing the waveguide was mounted in a small oven. Light of a HeNe laser (λ=633nm) was coupled into the waveguide by end-fire coupling with a microscope objective. The outcoupled light was detected with a photodiode and measured with a lock-in amplifier. Since $KNbO_3$ undergoes a phase transition at 220°C the annealing temperature must be kept beneath this value. The waveguide was heated up from room temperature to 150°C at a rate of 30°C/h and kept at 150°C for several hours until no further change of the transmission was observed. The slow heating rate was used in order to avoid depoling of the sample. The absolute value of the waveguide loss coefficient was measured after the annealing process by the optimum end-fire coupling method described in ref. [9].
Figure 1 shows the waveguide loss coefficient α at 633nm as a function of the anneling time. The sample temperature is shown below. The waveguide was implanted in a c-cut $KNbO_3$ crystal with an ion energy of 2.3 MeV and a dose of 1.5 x 10^{15}cm^{-2}. The data refer to a mode polarized along the b-axis (TE-mode). A decrease of the loss coefficient can be observed already during the heating period. The losses are further reduced as the waveguide is kept at 150°C. The improvement stops after approximately 7 hours. The long total annealing time of approximately 10 hours is a consequence of the necessity to keep the temperature relatively low. The final waveguide loss coefficient as measured after the annealing process at room temperature was 0.4cm^{-1} (1.7dBcm^{-1}).

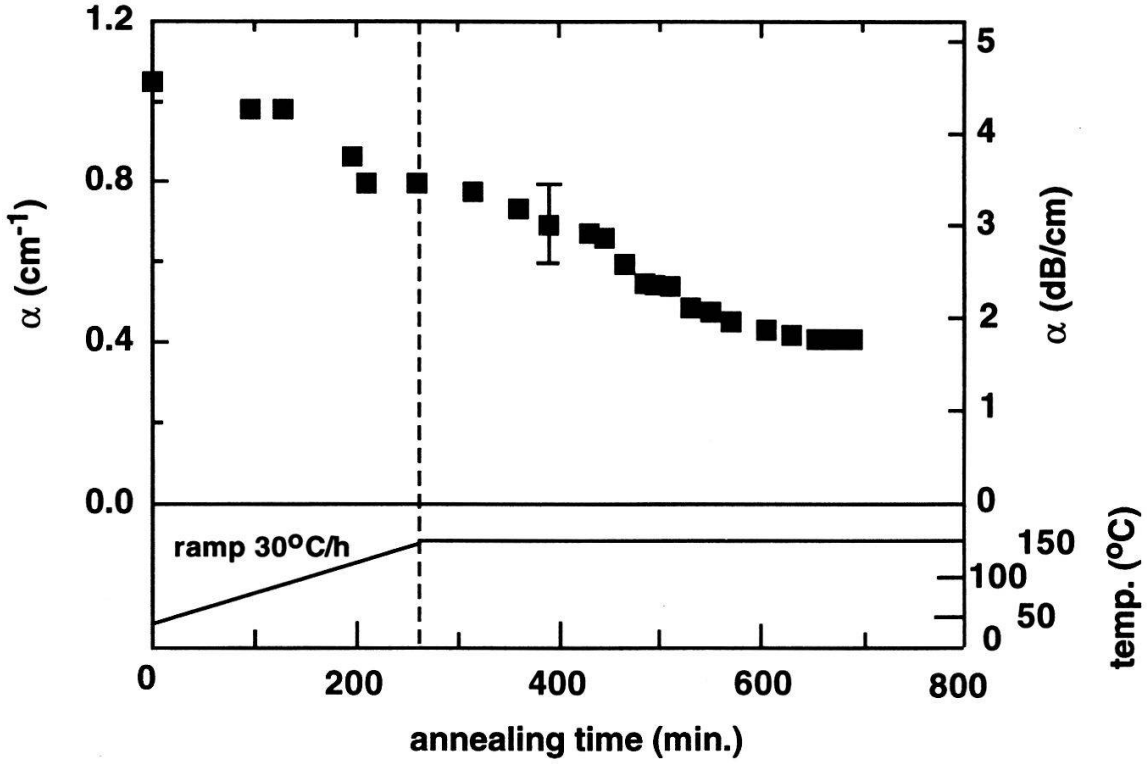

Fig. 1: Waveguide loss α at λ=633nm of an ion-implanted $KNbO_3$ channel waveguide (width 5.4μm, depth 5.0μm, length 0.74cm) as a function of the annealing time and temperature.

We also measured the waveguide loss coefficient before and after the annealing for several wavelengths. The coefficient was reduced by 1.0cm^{-1} at 454nm, 0.5cm^{-1} at 633nm and 0.2cm^{-1} at 860nm. Reduction of the losses was mainly achieved in the blue spectral range. The resulting loss coefficient after the annealing process was typically 1.8cm^{-1}, 0.7cm^{-1} and 1.3cm^{-1} at these wavelengths for TE-polarized modes.
The conversion efficiency for Cerenkov-type SHG was measured before and after the annealing process. In a 1.12cm long 5.4μm x 7.5μm channel waveguide 0.5mW of blue power at 433nm were produced with an infrared input power of 200mW at 866nm before annealing. After annealing 1.3mW of blue power were produced with the same input power. Thus the SH conversion efficiency of these ion implantated $KNbO_3$ channel waveguides was increased by more than a factor of two by a low-temperature post-implantation annealing process.

References

[1] P. Günter, Appl. Phys. Lett. **34**, 650 (1979)
[2] J.-C. Baumert, P. Günter, and H. Melchior, Opt. Commun. **48**, 215 (1983)
[3] T. Bremer, W. Heiland, B. Hellermann, P. Hertel, E. Krätzig, and D. Kollewe, Ferroelectrics Lett. **9**, 11 (1988)
[4] S. Schwyn Thöny, P. Günter, and H. W. Lehmann, Appl. Phys. Lett. **61**, 373 (1992)
[5] F.P. Strohkendl, D. Fluck, P. Günter, R. Irmscher, and Ch. Buchal, Appl. Phys. Lett. **59**, 3354 (1991)
[6] D. Fluck, P. Günter, M. Fleuster, and Ch. Buchal, J. Appl. Phys. **72**, 1671 (1992)
[7] D. Fluck, B. Binder, M. Küpfer, H. Looser, Ch. Buchal, and P. Günter, Opt. Commun. **90**, 304 (1992)
[8] D. Fluck, J. Moll, M. Fleuster, Ch. Buchal, and P. Günter, Electron. Lett. **28**, 1092 (1992)
[9] M. Haruna, Y. Segawa, and H. Nishihara, Electron. Lett. **28**, 1612 (1992)

A distributed temperature sensor based on multiphoton counting

M. Höbel, J. Rička, M. Wüthrich and T. Binkert

Institute of Applied Physics, University of Bern, Sidlerstr.5, 3012 Bern

We report on a fiberoptic distributed temperature sensor (DTS) which allows to measure simultaneously the temperature of up to 4000 points along an optical fiber. For the first time a DTS based on the multiphoton counting principle has been realized. We use 2ns laser diode pulses ($\lambda = 850$nm, $P = 500$mW) and a single photon avalanche diode (SPAD) as detector. One of the sensors' new features is the digital signal processing in real time with the new-developped multi time-interval analyzer MTIA-1. The spatial resolution of the prototype is 42cm with a maximum fiber length of 1600m.

Distributed temperature sensors allow to record the temperature profile along an optical fiber and can therefore replace a large number of single point thermometers [1] [2]. For this purpose a short laser pulse is injected into a multimode fiber and the operator measures the time dependent intensity of the Raman components of the backscattered light. The ratio R(T) of the Anti-Stokes and Stokes signals originating from a given fiber position depends on the temperature:

$$R(T) = (\frac{\lambda_s}{\lambda_{as}})^4 \; exp(-\frac{T_0}{T}) \qquad (1)$$

where λ_s and λ_{as} are the measured Stokes and Anti-Stokes wavelengths and T_0 depends on material properties of the sensor fiber. For a standard $50/125\mu$ multimode fiber T_0 takes a value of 634 K which results in a temperature sensitivity of about $0.8\%/°K$ at room temperature. Due to the extremely low Raman intensities the spatial resolution of a conventional DTS system is up to now limited to about 1 m. In this work we introduce the prototype of a distributed temperature sensor combining submeter spatial resolution with an acceptable measurement time. This is achieved with a multiphoton counting technique. In contrast to the conventional Single Photon Timing (SPT) method [3] time intervals between multiple stop signals related to one common start pulse can be processed. As a result the data acquisition time is reduced by two orders of magnitude. Fig. 1 illustrates the experimental setup of the prototype DTS-1. An anamorphotic optics couples laser diode pulses of 1-2 ns duration and 850 nm wavelength into a multimodefiber. Backscattered light from the sensor fiber is split in two branches where high quality interference filters extract the Raman components. A fiberoptic switch selects either Stokes or Anti-Stokes photons and directs the resulting extremely weak signal to the detector.

As the detector we chose an active quenched single photon avalanche diode (SPAD) which allows count rates of several MHz. With its 9 % photon detection probability and 500 mW coupled into the test fiber we observe 10-20 photons for each laser pulse. For an optimization of measurement time the digital processing of the multiple time intervals should be done in real time without interruption of the data acquisition.

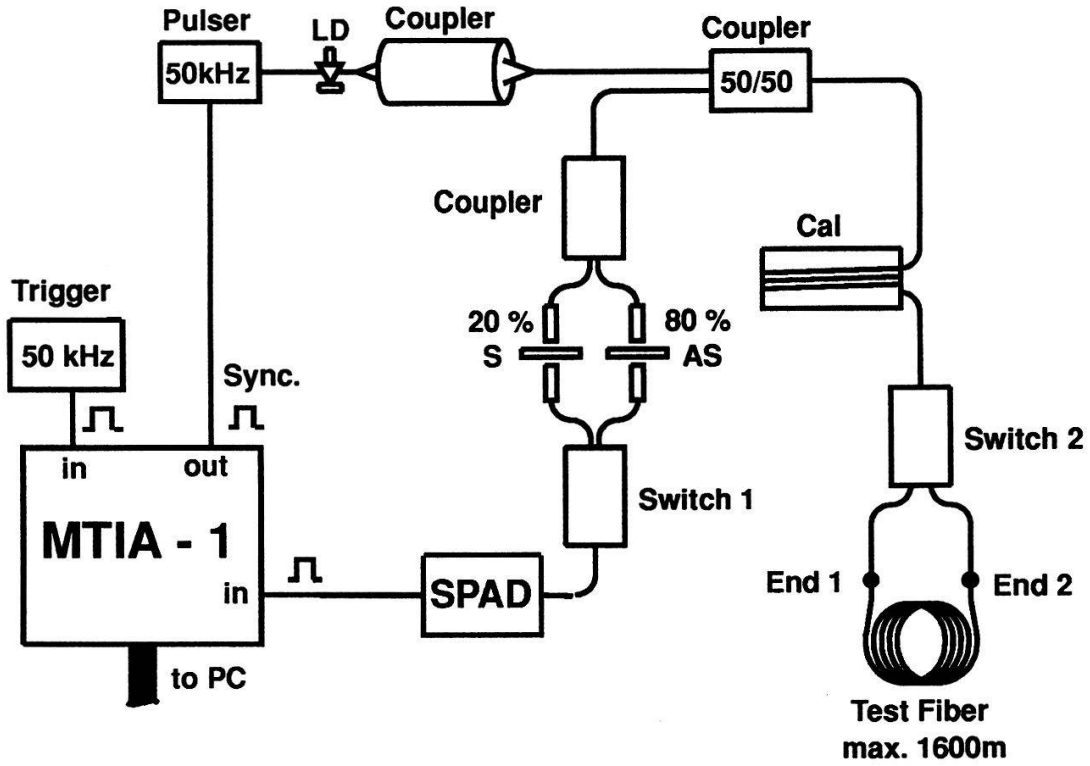

Figure 1: Experimental setup of the DTS-1

We developped the multi time-interval analyser MTIA-1 for this purpose [4]. The MTIA-1 uses a high speed logic and direct access to a superfast 4K*16 Bit RAM for real time signal processing. Incoming random pulse events are synchronized with the internal 240 MHz clock and increment the RAM at the adress corresponding to their time of occurance until the desired counting statistics is reached. The resulting histogramm of the detected counts in the MTIA channels reflect the time dependent intensity of the Raman components.

Experiments with the prototype demonstrated the spatial resolution of 42 cm for fibers up to 1600m long. The temperature accuracy depends on the measurement time. With the present configuration a $3\sigma = 4°$ C exactitude over the whole fiber distance may be obtained in about 10 minutes. This makes the DTS-1 attractive for a variety of surveillance or industrial process control applications [5] [6] .

References

[1] J.P.Dakin et al., Electr. Letters **21** , 569 (1985)

[2] A.H.Hartog et al., Electr. Letters **21** , 1061 (1985)

[3] R.Stierlin et al., Applied Optics **26**, 1368 (1987)

[4] M.Wüthrich and J.Rička, Eur. and US Patent Nr. P 4213717.9 (1992)

[5] H.Schad, Proc. of the SPIE, vol. 985, 64 (1989)

[6] M.A.Marcus, Proc. of the SPIE, vol. 1172, 194 (1989)

A MACROSCOPIC THEORY OF MELTING AND SOLIDIFICATION: NONLINEAR THERMAL DIFFUSION

P.W. Egolf and H. Manz

Swiss Federal Laboratories for Materials Testing and Research, 8600 Dübendorf

Many mixtures and glassy substances show a smooth transition of enthalpy as a function of temperature reaching from the pure solid to the pure liquid phase. A method to solve the melting and solidification problem of substances with a mushy region leads to a nonlinear thermal heat conduction equation with temperature-dependent coefficients. Differing from solutions of Burger's equation - where steepening is driven by a gradient - in our case, front creation occurs with a dependence on curvature.

Melting and solidification occur in many environmental and technical processes. An unique mathematical formulation of the macroscopic phenomenon is named Stefan problem, after J. Stefan, who was preoccupied in solidification of water in the polar sea at the end of the last century. F. Neumann found an analytical solution of the problem in the case of an isothermal semi-infinite domain and a discontinuous temperature change at its boundary. Enormous efforts in solving the Stefan problem by approximate analytical solutions have been made. Several methods like coordinate transformation, scaling techniques, reduction to integral equations, etc. led to useful solutions. In several practical cases, e.g. in solar engineering, the boundary conditions are stochastic or chaotic and therefore, during the last decade mostly applications of numerical methods have been performed. Very good results have often been obtained when an enthalpy formulation was applied (e.g. see ref. [1]). Taking existing theoretical treatments into consideration, these models and the overall specific heat method [2] proved to be very promising. The newly developed method is a combination and further development of these two methods.

As already mentioned, the aim was to construct a model, where the continuous transitions of all physical properties between the two phases solid and liquid (as a function of temperature) are taken advantage of. If energy conservation is formulated - including the law of Fourier for the heat flux density - we obtain:

$$\rho \cdot \frac{\partial h}{\partial t} + \frac{\partial}{\partial x}\left(-k\frac{\partial T}{\partial x}\right) = 0 \,. \tag{1}$$

The specific enthalpy and the heat conductivity k are temperature dependent properties. After performing an inner derivative and applying the product law of differential calculus, the result is:

$$\rho \cdot \frac{dh}{dT} \cdot \frac{\partial T}{\partial t} - k \cdot \frac{\partial^2 T}{\partial x^2} - \frac{\partial k}{\partial x} \cdot \frac{\partial T}{\partial x} = 0 \,. \tag{2}$$

For the whole temperature range the overall specific heat is defined as derivative of the specific enthalpy:

$$c_p = \frac{dh}{dT}, \qquad h = \int_0^T c_p(T')dT'. \tag{3}$$

We assume a constant density ρ. With equation (3) we obtain the following nonlinear diffusion equation with the temperature dependent coefficients:

$$\frac{\partial T}{\partial t} = a(T)\cdot\frac{\partial^2 T}{\partial x^2} + b(T)\cdot\left(\frac{\partial T}{\partial x}\right)^2, \tag{4}$$

$$a(T) = \frac{k}{\rho\cdot c_p}, \quad b(T) = a(T)\cdot\frac{1}{k}\cdot\frac{dk}{dT}.$$

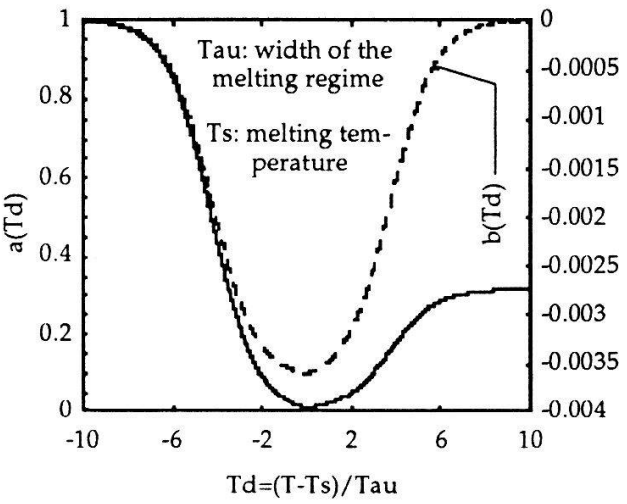

Figure 1: Example of temperature dependent nonlinear functions occurring in equation (4).

In chemistry with constant coefficients this type of equation is known as phase diffusion equation. Because a square product of the spatial derivative occurs, it is nonlinear even when the coefficients are considered constant. It describes front propagations in diffusion-limited reaction diffusion systems [3,4].

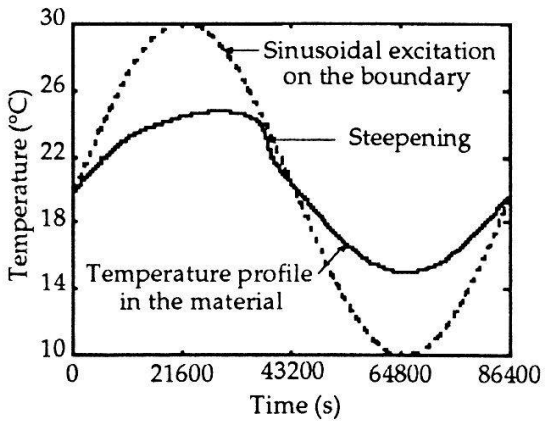

Figure 2: Steepening process of a temperature distribution in the bulk of the material.

Another interesting analogy occurs to phenomena in fluid dynamics. Via the Cole-Hopf transformation Burger's equation is obtained:

$$v = -2b\frac{\partial T}{\partial x} \Rightarrow \frac{\partial v}{\partial t} = a\frac{\partial^2 v}{\partial x^2} - v\frac{\partial v}{\partial x}, \tag{5}$$

which is known to have a family of shock solutions. In phase change materials - analogous to the steepening of fluiddynamical waves - steepening of temperature distributions can be observed (figure 2). In our case, because of the temperature dependence of the coefficients, other front positions as function of time result.

[1] V.R. Voller, 1990, Numerical Heat Transfer, **17B**, 155
[2] M. Nishimura, Y. Bando, M. Kuraishi and W.P. Hahne, 1987, Kagaku Kogaku Ronbunshu **13/4**, 435
[3] Y. Kuramoto, *Chemical oscillations, waves and turbulence*, 1984, Springer-Verlag
[4] L. Galfi and Z. Racz, 1988, Phys. Rev. A **38/6**, 3151

SCATTERING OF INTERSTELLAR HELIUM ATOMS IN THE EARTH'S ATMOSPHERE

M. BASSI AND F. BÜHLER

Physikalisches Institut, University of Bern, 3012 Bern

The scattering of the neutral interstellar He atoms in the atmosphere was analytically calculated. Most important are binary collisions with neutral oxygen atoms, thus only these have been considered. The resulting angular distribution strongly depends on altitude, local time, solar activity, and incidence angle of the He atom.

Unsere Gruppe wird 1994/95 auf einem russischen Satelliten ein Experiment zum Sammeln von interstellarem Gas durchführen (COLLISA – Collecting of Interstellar Atoms). Dabei bedienen wir uns der Foliensammeltechnik, d.h. wir bringen dünne Folien auf einige hundert Kilometer Höhe, wo sie dem Beschuss der neutralen Atome des interstellaren Gases ausgesetzt werden.

Bevor die interstellaren Atome auf die Folien treffen, müssen sie die oberen Schichten der Atmosphäre durchqueren. Dabei werden sie durch Stösse mit den Atmosphärenteilchen (hauptsächlich mit neutralem atomarem Sauerstoff) abgelenkt und verlieren kinetische Energie. Unsere Arbeit hatte den Zweck, den Einfluss der genannten Effekte auf unser Experiment abzuschätzen.

Für den Stossprozess nahmen wir den klassischen elastischen Stoss zweier neutraler Atome an. Das bedeutet unter anderem, dass keine relativistischen Geschwindigkeiten und keine inelastischen Prozesse wie Ionisation oder Hüllenanregung auftreten dürfen. Die Wechselwirkung der beiden Atome beschrieben wir durch das *Universale Potential* von Ziegler, Biersack und Littmark [1]. Es gehört zu den abgeschirmten Coulomb-Potentialen, bei welchen ein Coulomb-Term die Wechselwirkung der elektrischen Kernladungen beschreibt und eine Abschirmfunktion die Abschirmung der Kernladungen durch die Hüllenelektronen berücksichtigt.

Die Wellennatur und die Polarisation der Atome werden dabei nicht einbezogen. Dennoch zeigt das Universale Potential eine gute Übereinstimmung mit theoretisch und experimentell bestimmten Potentialen [2]. Für die Berechnung des Ablenkwinkels Θ bei einem Stoss benutzten wir die *Magische Formel* von Biersack und Haggmark [3]. Dies ist ein analytischer Ausdruck für Θ, der an das gewählte Potential angepasst werden muss.

Als *Streuwinkel nach dem N-ten Stoss* ϱ_N bezeichnen wir den Winkel zwischen der ursprünglichen Flugbahn, dh. der Flugbahn vor dem ersten Stoss, und der aktuellen Flugbahn. Er berechnet sich rekursiv aus dem vorherigen Streuwinkel ϱ_{N-1}. Wir haben numerisch für die ersten 10 Stösse die Streuwinkelverteilung von atomarem He (mit atomarem ^{16}O als Stosspartner) berechnet. Da der klassische Stossquerschnitt unendlich gross ist, stellten wir an einen Stoss die zusätzliche Bedingung, dass er zu einer Ablenkung von mindestens 0.01 rad

	N									
	1	2	3	4	5	6	7	8	9	10
^{3}He	86.8	74.8	64.2	54.9	47.0	40.3	34.7	30.0	26.0	22.7
^{4}He	87.8	76.6	66.5	57.6	49.8	43.1	37.5	32.7	28.6	25.2

Tabelle 1: Prozentsatz der He-Atome (15eV/Nukleon), die nach N Stössen mit neutralem atomarem Sauerstoff einen Streuwinkel unter 20^o Grad haben.

	Einfallswinkel in Grad							
	Sonnenminimum				Sonnenmaximum			
Höhe [km]	0	20	40	70	0	20	40	70
200	16.9	18.0	22.0	47.3	66.1	70.2	85.7	182
300	2.2	2.3	2.8	6.1	16.9	17.9	21.9	45.9
400	0.34	0.36	0.44	0.93	4.7	5.0	6.1	13
500	0.05	0.05	0.07	0.14	1.3	1.4	1.7	3.6

Tabelle 2: Anzahl Stösse von interstellarem ^{4}He (15eV/Nukleon) mit neutralem atomarem Sauerstoff der Atmosphäre für verschiedene Endhöhen und Einfallswinkel der Flugbahn.

(= 0.57^o) führen sollte. Ausserdem schätzten wir den Energieverlust ab. Für die He-Atome mit einem Streuwinkel unter 20^o nach dem letzten Stoss (s. Tabelle 1) ist er sogar noch nach 10 Stössen vernachlässigbar. Nur diese Atome interessieren uns, denn die stärker gestreuten werden in unserem Experiment abgeschirmt.

Mittels der MSIS 86 - Referenzatmosphäre bestimmten wir die zu erwartende Anzahl Stösse für ^{4}He-Atome mit einem kleinen Streuwinkel nach dem letzten Stoss (Tabelle 2). Sie hängt hauptsächlich von der Sonnenaktivität, der Höhe, dem Einfallswinkel und der Ortszeit ab. So müsste man z.B. am 19.2.79 mittags (während einer Periode hoher Sonnenaktivität) auf 400 km Höhe rund 14 mal mehr Stösse erwarten als am 13.7.76 mittags, als die Sonnenaktivität niedrig war. Ausserdem zeigt Tabelle 2 einen starken Anstieg der Anzahl Stösse ab einem Einfallswinkel von 40^o. Für ^{3}He sind die Werte 13% höher.

Mit den Zahlen aus den beiden Tabellen 1 und 2 schätzten wir den Prozentsatz der ^{4}He-Atome, die mehr als 20^o gestreut werden (und damit für unser Experiment verloren sind), bevor sie die Satellitenhöhe erreichen. Für senkrechten Einfall und die erwähnte Sonnenminimum-Atmosphäre sind das auf 400 km Höhe 4%, für die Sonnenmaximum-Atmosphäre dagegen 45% ! Für ^{3}He betragen die Verluste 5% bzw. 53%.

Literaturverzeichnis

[1] J.F.Ziegler, J.P.Biersack, U.Littmark, "The Stopping and Range of Ions in Solids", Vol. 1, Pergamon Press New York (1985)

[2] D.J.O'Connor, J.P.Biersack, Nucl. Instr. and Meth. **B 15**, 14 (1986)

[3] J.P.Biersack, L.G.Haggmark, Nucl. Instr. and Meth. **174**, 257 (1980)

Verhalten von Flüssigkristall-Monolayern an der Grenzfläche Wasser-Luft

Th. Enderle, I. Amstutz, A.J. Meixner und I. Zschokke-Gränacher
Institut für Physik, Universität Basel, Klingelbergstrasse 82, 4056 Basel

In den vergangenen Jahren hat die Untersuchung der physikalischen, insbesondere optischen Eigenschaften von Langmuir-Filmen und Langmuir-Blodgett-Filmen in zunehmendem Mass an Bedeutung gewonnen [1]. Im Hinblick auf die zukünftige Anwendung dieser monomolekularen Filme ist es unerlässlich, die Phasenübergänge besser zu verstehen, die bei der Ordnung von amphiphilen Molekülen zu einem Langmuir-Film auf einer Wasseroberfläche durchlaufen werden. In Monolayern aus Stearinsäure und 4-n-octyl-4'-cyanobiphenyl (8CB) haben wir neben der üblichen Filmdruckmessung auch die Orientierung d.h. den Neigungswinkel der 8CB Moleküle zur Wasseroberfläche mit Hilfe der optischen Frequenzverdoppelung (SHG) bestimmt. Aus der simultanen Messung von Filmdruck und SHG-Intensität während dem Komprimieren des Films erhält man somit detaillierte Informationen über die Ordnung und die Orientierung der 8CB-Chromophoren im Monolayer [2–4]. Der Bildungsprozess von reinen und gemischten 8CB-Monolayern lässt sich in 4 Bereiche unterteilen (vgl. 1 bis 4 in Abbildung 1):

1. Unterhalb eines Filmdrucks von 0.05 mN/m ist das SHG Signal Null, was auf eine unpolare Orientierung der 8CB-Chromophoren schliessen lässt.
2. Bei einem Filmdruck von etwa 0.05 mN/m beginnt ein Phasenübergang zu einer polar orientierten Phase. Der Neigungswinkel der Längsachse der 8CB-Moleküle zur Filmnormalen beträgt hier 57° (vgl. Abbildung 2).
3. Weiteres Komprimieren des Monolayers führt unter starkem Anstieg des Filmdrucks zu einer Verdichtung der polaren Phase. Gleichzeitig nimmt der Neigungswinkel ab, d.h. die Moleküle richten sich weiter auf (vgl. Abbildung 2).
4. Oberhalb eines kritischen Filmdrucks (etwa 7 mN/m beim reinen 8CB-Film) folgt schliesslich ein Phasenübergang in eine zentrosymmetrische Anordnung der 8CB-Moleküle, was sich in einer Abnahme der SHG-Intensität äussert. Der Wert dieses kritischen Drucks nimmt mit zunehmendem Stearinsäureanteil zu, d.h. die 8CB-Moleküle werden durch die Stearinsäure stabilisiert.

Abbildung 2 zeigt weiterhin, dass trotz des Stabilisierungseffekts durch die Stearinsäure die Orientierung der 8CB-Moleküle im gemischten Film nur vom Filmdruck und nicht vom Mischungsverhältnis mit Stearinsäure abhängt.

Dieses Projekt wird durch den Schweizerischen Nationalfonds unterstützt.

Literaturangaben:

1. A. Ulman, *Ultrathin Organic Films*, (Academic Press New York, 1991), Kapitel 5
2. J. Xue et al., Phys.Rev.Lett, 69, 474 (Juli 1992)
3. M. Barmentlo et al., Chem.Phys.Lett., 209, 347 (Juli 1993)
4. Th. Enderle et al., Mol.Cryst.Liq.Cryst., in Druck

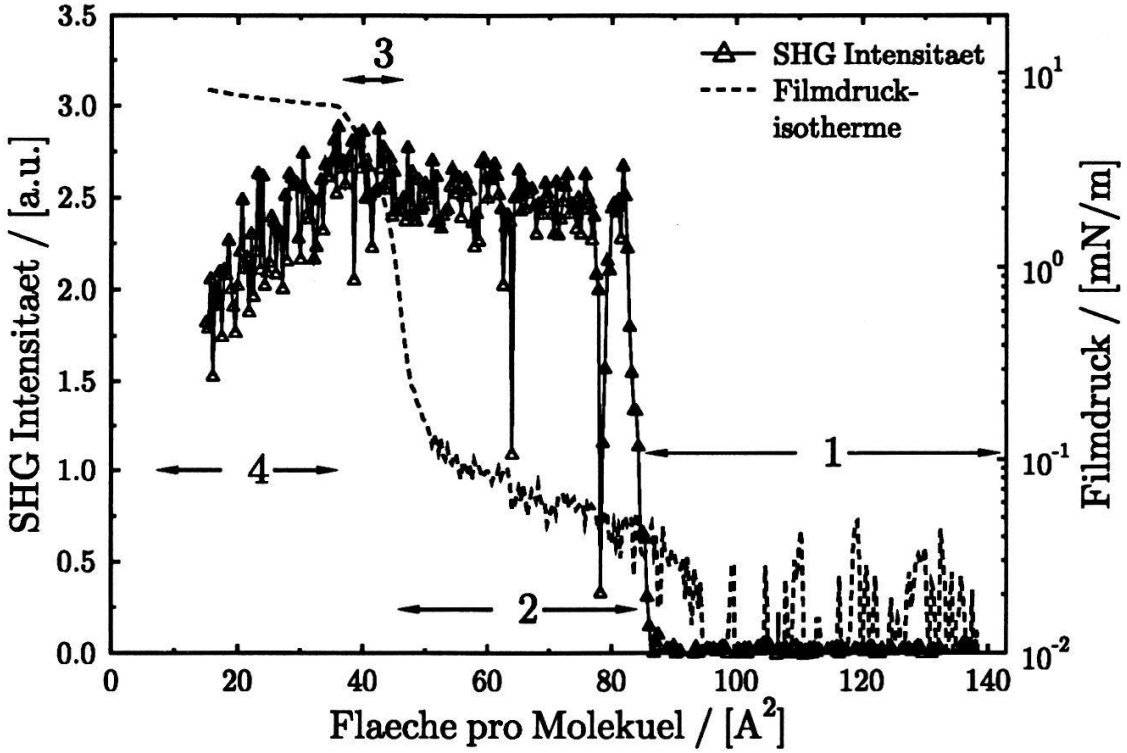

Abbildung 1: Bildung eines Monolayers aus reinem 8CB bei Raumtemperatur. Die Dreiecke stellen den s-polarisierten Anteil der SHG-Intensität dar, bei einer Polarisation der eingestrahlten Grundwelle von 45°. Die gestrichelte Linie ist die logarithmische Darstellung der gleichzeitig gemessenen Filmdruckisotherme.

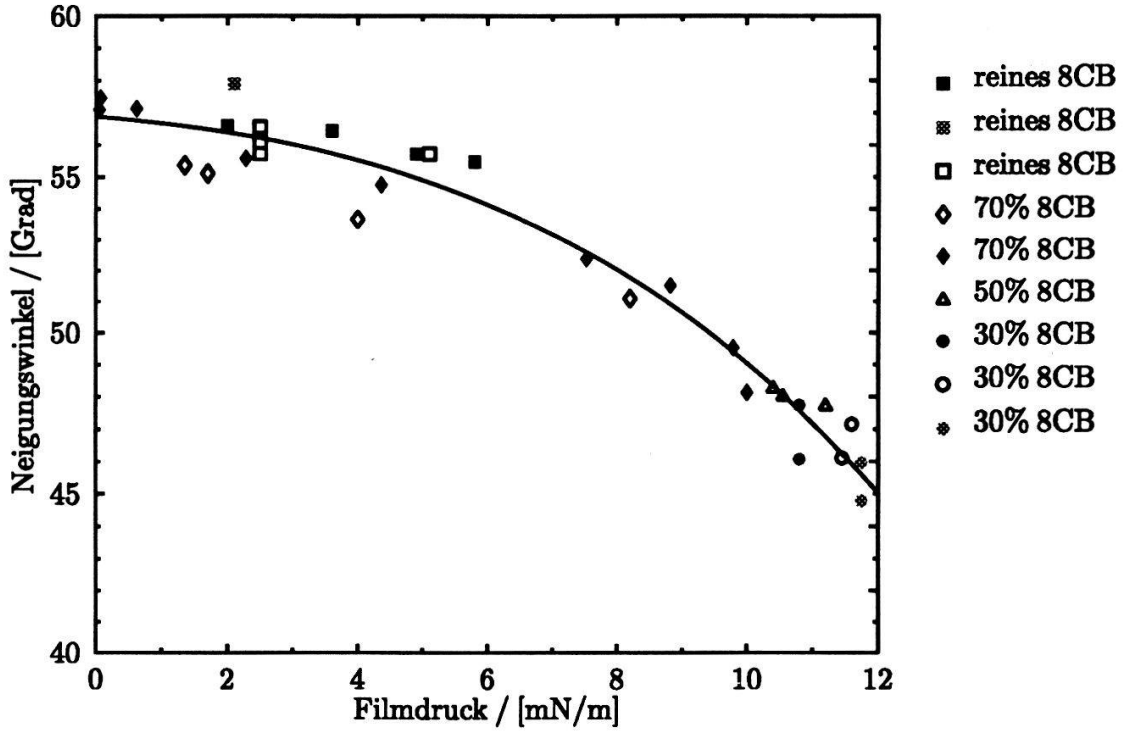

Abbildung 2: Neigungswinkel der 8CB-Moleküle zur Filmnormalen als Funktion des Filmdrucks für reine und gemischte Monolayer. In gemischten Filmen werden höhere Filmdrücke erreicht und die 8CB Moleküle nehmen deshalb aufrechtere Positionen (bis zu 45°) ein.

Muon capture ratio A(Ar,Ne) in gaseous mixtures Ar + Ne

Y.-A. Thalmann, O. Huot,, R. Jacot-Guillarmod, F. Mulhauser, C. Piller, L.A. Schaller, L. Schellenberg, H. Schneuwly and A. Werthmüller

Institut de physique de l'Université, CH-1700 Fribourg, Switzerland

Muons decelerated in matter are finally captured by the Coulomb fields of nuclei: they form muonic atoms. By using the Lyman series intensities of the characteristic muonic X-rays, one determines muon capture ratios. This ratio has been measured three times in 1:1 gaseous mixtures Ar + Ne at 15 bar. The mean value of the ratios is A(Ar,Ne) = 1.25 ± 0.05.

The atomic capture of negative muons is investigated since already about thirty years and, during this time, numerous experimental data have been produced, especially in chemical compounds in solid state. In spite of all these data, none of the various models proposed for the muon capture process is able to reproduce the measured data in a really satisfactory manner.

Pion capture measurements in hydrogen compounds have shown that the chemical bond plays a decisive role in the capture mechanism. In hydrogen compounds or mixtures, there is in addition transfer of the pion (or muon) to other elements such that the chemical bond effects cannot be identified without a certain ambiguity. In muon capture in solid compounds, the influence of the chemical bond on the capture by an element cannot be suppressed nor clearly identified. The investigation of noble gases is the only way to study muon capture free from chemical bond effects.

For this reason, we have investigated the capture of negative muons in 1:1 mixtures of Ne + Ar at room temperature at a pressure of 15 bar. The measurements have been performed at the μE4 channel at PSI by using the usual experimental set-up described elsewhere [1].

Three measurements have been performed, the first one in December 1988 and the two others in March 1993. The muonic X-ray intensity patterns of neon and argon of all three measurements agree well with each other. They agree also with the patterns, measured in pure gases, reported by Ehrhart et al. [2] and by Jacot-Guillarmod et al [3].

Because the spatial muon stop distribution inside the gas target is not known with precision, the absorption of the target walls has been studied in a separate experiment. The efficiency of the detection system and the transmission, which have been measured by using a set of radioactive sources of known relative intensities, has been checked by comparing the muonic intensities of the Balmer series in argon with the prediction of a muon cascade calculation which reproduces the measured intensities of the Lyman series [3].

The relative intensities of the Lyman series of both neon and argon can be reproduced by assuming a statistical angular momentum distribution in the muon-atomic level of main quantum number n = 14, where the cascade calculation is started. Energetically, the Lyman series of the muonic neon X-rays and the Balmer series of the muonic argon X-rays overlap. If, in argon, the calculated intensities of the Balmer series relative to those of the Lyman series agree with the

measured ones, one can assume that the efficiency and transmission of the experimental set-up for the Lyman series of neon relative to those of argon have been correctly determined.

The muon capture ratio is determined by summing up the intensities of the muonic X-rays of the Lyman series in argon and in neon such that

$$A(Ar,Ne) = \frac{\sum_n I_{Ar}(n-1)}{\sum_n I_{Ne}(n-1)}$$

defines the capture ratio. The measured ratios are given in the Table together with the result obtained by Ehrhart et al. [2] ten years ago.

Measurement	Pressure	A(Ar,Ne)	Reference
December 1988	15 bar	1.27 ± 0.05	this work
March 1993 (a)	15 bar	1.28 ± 0.05	this work
March 1993 (b)	15 bar	1.20 ± 0.05	this work
Ehrhart et al.	51 bar	1.01 ± 0.05	[2]

Our three independent A(Ar,Ne) capture ratios, measured at a total pressure of 15 bar, agree with each other. They disagree, however, with the one measured by Ehrhart et al. in a 1 : 1 mixture at 50 bar. It has already been reported that muon capture ratios in noble gases depend on the relative concentrations [2]. That such capture ratios might depend on the total pressure is not expected.

References

[1] R. Jacot-Guillarmod, F. Bienz, M. Boschung, C. Piller, L.A. Schaller, L. Schellenberg, H. Schneuwly, W. Reichart and G. Torelli, Phys. Rev **A 38** (1988) 6151.
[2] P. Ehrhart, F.J. Hartmann, E. Köhler and Daniel, Z. Physik **A 311** (1983) 259.
[3] R. Jacot-Guillarmod, F. Bienz, M. Boschung, C. Piller, L.A. Schaller, L. Schellenberg, H. Schneuwly and D. Siradovic, Phys. Rev. **A 37** (1988) 3795.

THEORY OF THE FEMTOSECOND DYNAMICS OF THE LASER-INDUCED LATTICE INSTABILITY OF Si AND GaAs

P. Stampfli and K.H. Bennemann

Institute for Theoretical Physics, Freie Universität Berlin,
Arnimallee 14, D-14195 Berlin, Germany

We analyze the femtosecond instability of the diamond lattice of silicon and GaAs, which is induced by a dense electron-hole plasma after excitation by a very intense laser pulse. We present results for the time-dependence of the instability for the case where 15% of the valence electrons have been excited into the conduction band. Thus, already 100 fsec after the excitation of the plasma the atoms are displaced about 1Å from their equilibrium position and their kinetic energy has increased to approximately 0.4 eV. Collisions between the atoms then lead to a rapid melting of the crystal. These results are in good agreement with recent experiments.

In our previous work[1,2] we have shown that a very dense laser-generated electron-hole plasma results in an instability of the transverse acoustic phonons of the diamond structure of Si and related semiconductors (GaAs). Here we introduce additional longitudinal optical phonon distortions, which enhance the instability of the acoustic phonons.

We consider the transverse acoustic phonon at the L-point[2]. The wave vector is $\mathbf{k}_L = \pi(1,1,1)/3a_o$, where a_o is the lattice constant of the fcc unit cell of the diamond structure. The displacement of an atom is $\pm\delta_t \mathbf{e}_t$, where $\mathbf{e}_t = (1,1,-2)/\sqrt{6}$ is a transverse polarization vector and the sign depends on the position of the atom. This phonon has a strong anharmonic interaction with the longitudinal optical phonon at the Γ-point because of the electron-hole plasma. The atomic displacements of the longitudinal optical phonon are $\pm\delta_\ell \mathbf{e}_\ell$, where $\mathbf{e}_\ell = (1,1,1)/\sqrt{3}$ is the longitudinal polarization vector.

The cohesive energy per atom $E_b(\delta_t, \delta_\ell)$, see refs. 1 and 2 for more details, is obtained from a tight-binding Hamiltonian for the electronic density of states $\rho(\varepsilon)$. The highly excited electron gas (electron-hole excitation density $> 1 \times 10^{22}\mathrm{cm}^{-3}$) thermalizes on a time scale of 10 fsec, which is much faster than the the movement of the atoms (time scale: 100 fsec). Thus it has a well defined temperature T_e. Heat exchange with the lattice is slow (time scale: several psec) and can be neglected here. Thus, the entropy S_e of the electron gas remains constant ($\delta Q = T\, dS_e = 0$) and determines the electronic temperature T_e. Without laser excitation ($S_e = 0$) this theory is equivalent to the Born-Oppenheimer approximation.

On the left of Fig. 1 we present our results for the cohesive energy per atom $E_b(\delta_t, \delta_\ell)$ of Si as a function of the amplitudes of the transverse acoustic and longitudinal optical phonon. In this case 15% of the electrons have been excited from the valence band into the conduction band. Thus the diamond structure ($\delta_t = \delta_\ell = 0$) has become an unstable saddle point of the cohesive energy surface. A deep valley opens, leading down to very large negative energies of $E_b \cong -0.45$ eV for large δ_t and δ_ℓ. Note that neglecting longitudinal optical phonons (putting $\delta_\ell \equiv 0$) gives a much shallower minimum[2] of $E_b \cong -0.16$ eV. Using $E_b(\delta_t, \delta_\ell)$ as an effective potential we obtain the time-dependence of the average displacement $d(t)$ of the atoms from their initial position and the average kinetic energy $E_{kin}(t)$ as shown on the left of fig. 1. Note that within 120 fsec the kinetic energy of the atoms becomes larger than

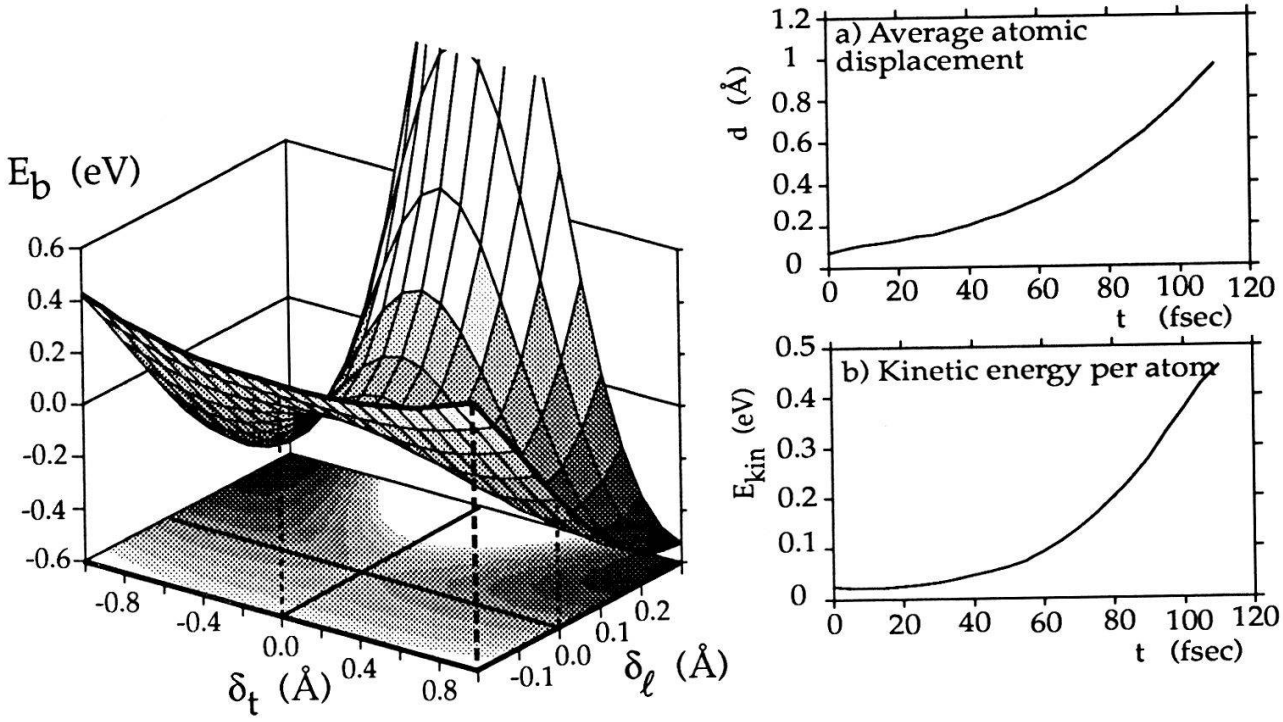

Fig. 1, on the left: Cohesive energy per atom E_b of Si shown as a function of the transverse acoustic distortion δ_t and the longitudinal optical distortion δ_ℓ of the diamond lattice. Note that 15% of the valence electrons have been excited into the conduction band. Thus the ideal diamond structure ($\delta_t = \delta_\ell = 0$) has become an unstable saddle point. On the right: (a) Time-dependence of the average displacement $d(t)$ of the atoms from their position in the ideal diamond lattice. (b) Time-dependence of the average kinetic energy $E_{kin}(t)$ of the atoms.

0.4 eV, corresponding to a temperature far above the melting temperature of Si. In the same time, the atomic displacements increase to about 1 Å, which is roughly half the bond length in Si. Thereafter collisions between the atoms lead to a very rapid melting of the crystal.

These results also apply to GaAs because of dominant tetrahedral covalent bonding. The larger mass of the atoms and the slightly larger bond length results in a slower movement. This increases the time required for the instability to about 200 fsec. Thus, we obtain a good quantitative agreement with recent experiments performed on Si and GaAs[3-6].

References

[1] P. Stampfli and K.H. Bennemann, Phys. Rev. B **42**, 7163 (1990)
[2] P. Stampfli and K.H. Bennemann, Phys. Rev. B **45**, 10686 (1992)
[3] S.V. Govorkov, T. Schroder, I.L. Shumay and P. Heist, Phys. Rev. B **46**, 6864 (1992)
[4] P. Saeta, J.-K. Wang, Y. Siegal, N. Bloembergen and E. Mazur, Phys. Rev. Lett. **67**, 1023 (1991)
[5] K. Sokolowski-Tinten, H. Schulz, J. Bialowski and D. von der Linde, Appl. Phys. A **53**, 227 (1991)
[6] H.W.K. Tom, G.D. Aumiller and C.H. Brito-Cruz, Phys. Rev. Lett. **60**, 1438 (1988)

Local Scale Invariance in Strongly Anisotropic Critical Systems

Malte Henkel

Département de Physique Théorique, Université de Genève, 1211 Genève 4

Strongly anisotropic scaling occurs in many equilibrium and non-equlibrium statistical systems. We propose to extend the dynamical scaling hypothesis to include some kinds of local, space-time dependent scaling transformations as well. For the special case of a dynamical exponent $z = 2$, we consider the Schrödinger group as the group of local scale transformations. Two- and three-point correlation functions are found for either fully infinite or half-infinite space-time. The results can be reproduced in several exactly solvable strongly anisotropic critical systems.

The notion of scale invariance is a central one in modern theories of critical behaviour. In particular, for two-dimensional and isotropic equilibrium systems, the extension of scale invariance to conformal invariance [1] has led to an explosion of knowledge about these systems. Here, we consider strongly anisotropic critical systems, for which by definition the (connected) correlation function $C(\vec{r};t)$ depending on "space" distances r and "time" distances t satisfies

$$C(\lambda r;\lambda^\theta t) = \lambda^{-2x} C(r;t) \tag{1}$$

where x is a scaling dimension and $\theta \neq 1$ is the anisotropy exponent (often denoted by z and called dynamical exponent). While this is usually taken to hold for λ constant, we propose to consider conveniently chosen *space-time dependent* scale transformations $\lambda(r,t)$.

The simplest non-trivial example appears to arise for $\theta = 2$. The group of scale transformation we consider is the Schrödinger group found independently by Niederer [2] and Hagen [3]. It is known that the free Schrödinger equation and also free non-relativistic field theory is invariant under the transformations (here we consider only $d = 1$ space dimension for brevity, with immediate generalization to d arbitrary)

$$r \to r' = \frac{r + vt + a}{\gamma t + \delta} \quad , \quad t \to t' = \frac{\alpha t + \beta}{\gamma t + \delta} \quad ; \quad \alpha\delta - \beta\gamma = 1 \tag{2}$$

where $\alpha, \beta, \gamma, \delta, v, a$ are real parameters. Some care is needed since the wave functions also pick up an additional phase under these transformations [2, 3] which contain the (non-relativistic) mass $\mathcal{M}$ of the field. The Schrödinger Lie algebra is spanned by the generators $X_{\pm 1}, X_0, Y_{\pm 1/2}, M_0$ [4], where $M_n = -t^n \mathcal{M}$ and (for Euclidean times)

$$\begin{aligned} X_n &= -t^{n+1}\partial_t - \frac{n+1}{2} t^n r \partial_r - \frac{n(n+1)}{4} \mathcal{M} t^{n-1} r^2 \\ Y_m &= -t^{m+1/2}\partial_r - \left(m + \frac{1}{2}\right) \mathcal{M} t^{m-1/2} r \end{aligned} \tag{3}$$

Scaling fields ϕ (in $d = 1$ space dimension) are then characterized by their scaling dimension x and mass $\mathcal{M}$.

We now require a multipoint correlation function to transform covariantly under the action of the Schrödinger group. We first consider the case that both time and space are infinite in extent. The two-point function is then completely determined [5]

$$F_2 =< \phi_a(r_a,t_a)\phi_b^*(r_b,t_b) >= \delta_{x_a,x_b}\delta_{\mathcal{M}_a,\mathcal{M}_b}\Phi_0(t_a-t_b)^{-x_a}\exp\left[-\frac{\mathcal{M}_a}{2}\frac{(r_a-r_b)^2}{t_a-t_b}\right] \quad (4)$$

where Φ_0 is a normalization constant, while for the three-point function $F_3 =< \phi_a\phi_b\phi_c^* >$

$$F_3 = \delta_{\mathcal{M}_a+\mathcal{M}_b,\mathcal{M}_c}(t_a-t_c)^{-\frac{1}{2}(x_a+x_c-x_b)}(t_b-t_c)^{-\frac{1}{2}(x_b+x_c-x_a)}(t_a-t_b)^{-\frac{1}{2}(x_a+x_b-x_c)} \quad (5)$$
$$\times \exp\left[-\frac{\mathcal{M}_a}{2}\frac{(r_a-r_c)^2}{t_a-t_c}-\frac{\mathcal{M}_b}{2}\frac{(r_b-r_c)^2}{t_b-t_c}\right]\Psi_{ab,c}\left(\frac{[(r_a-r_c)(t_b-t_c)-(r_b-r_c)(t_a-t_c)]^2}{(t_a-t_b)(t_a-t_c)(t_b-t_c)}\right)$$

where $\Psi_{ab,c}$ is an arbitrary function. We recognise the appearance of the Bargmann superselection rule for the masses. For a half-infinite space ($r \geq 0$) we have [5]

$$F_2 = \delta_{x_a,x_b}(t_a-t_b)^{-x_a}\chi_{a,b}\left(\frac{r_a r_b}{t_a-t_b}\right)\exp\left[-\frac{\mathcal{M}_a}{2}\frac{r_a^2}{t_a-t_b}-\frac{\mathcal{M}_b}{2}\frac{r_b^2}{t_a-t_b}\right] \quad (6)$$

with $\chi_{a,b}$ arbitrary. For times restricted to $t \geq 0$ and infinite space

$$F_2 = \delta_{\mathcal{M}_a,\mathcal{M}_b}t_a^{-(x_a+x_b)/2}\Phi_{a,b}(t_a/t_b)\exp\left(-\frac{\mathcal{M}_a}{2}\frac{(r_a-r_b)^2}{t_a-t_b}\right) \quad (7)$$

where $\Phi_{a,b}$ is an arbitrary function.

These results can be reproduced from several exactly solvable models with $\theta = 2$ (or $z = 2$). These models are the $1D$ kinetic Ising model with Glauber dynamics, lattice diffusion with parallel updating, the dynamic spherical model with a non-conserved order parameter and the Lifshitz point (of first order) in the spherical model, see [5] for details.

Finally, we briefly recall that it had been tried to extend (1) by using the conformal group [6] as a group of local scale transformations. That approach had yielded the two-point function for arbitrary values of θ. While it agrees with our result for $\theta = 2$, the form found for generic values of θ apparently is in disagreement with exact results for Lifshitz points of higher order in the spherical model as well as from directed percolation (see [5]).

This work was supported in part by the Swiss National Science Foundation.

References

[1] A.A. Belavin, A.M. Polyakov and A.B. Zamolodchikov, Nucl. Phys. **B241**, 333 (1984)

[2] U. Niederer, Helv. Phys. Acta **45**, 802 (1972)

[3] C.R. Hagen, Phys. Rev. **D5**, 377 (1972)

[4] M. Henkel, Int. J. Mod. Phys. **C3**, 1011 (1992)

[5] M. Henkel, Geneva preprint UGVA-DPT 1993/09-833

[6] J.L. Cardy, J. Phys. **A18**, 2771 (1985)

CAN A SYSTEM AT CURIE TEMPERATURE REMAIN NONRECIPROCAL EVEN FOR SIGNALS ENSUING FROM ESPECIALLY TREATED THERMAL NOISE?

J.SANDTNER
Sonnenweg 10, CH-4436 Oberdorf

Abstract: Small number of reactance networks discoupled with power combiners can redistribute noise energy along the time axis so that equivalent noise temperatures of several thousands K might be attained during a finite time. Recurrence time of such rare events can be shortened. Rayleigh hysteresis loop nonlinearity of a ferrite rod at temperatures near its Curie point serves for a low dissipation frequency converter. Perhaps, such systems can remain nonreciprocal even for signals of thermal noise magnitudes.

Theory: Since noise energy can be stored in pure reactances, small number of reactance networks can redistribute noise energy along the time axis. An LC resonator represents one degree of freedom which corresponds to one gas molecule in a one-dimensional space. If coupled circuits are used, the number of degrees of freedom is reduced in accordance with Kirchhoff's laws. Reactances with a frequency characteristics and autocorrelation function, both having a Gaussian shape, may be used.
Power combiner is a linear four-port described by a cascade matrix. If two output ports are terminated with identic impedances then inputs are independent. As it is a linear network, it is supposed, that a power combiner behaves in this way even for signal magnitudes comparable with those of thermal noise.

FIG.1 POWER COMBINER NETWORK WITH A NONLINEARITY.

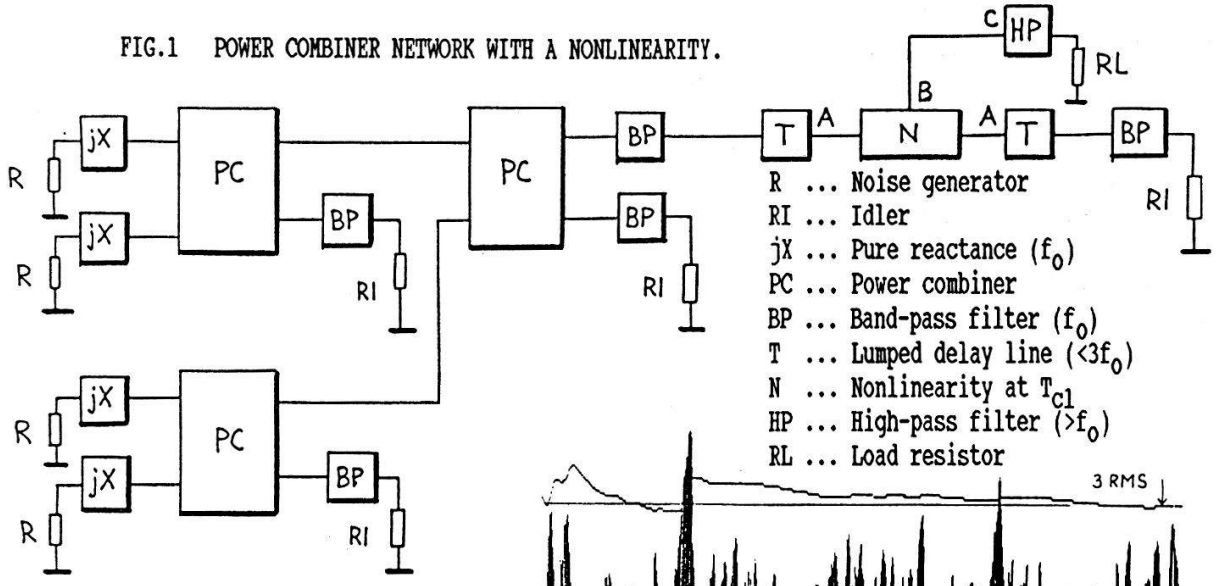

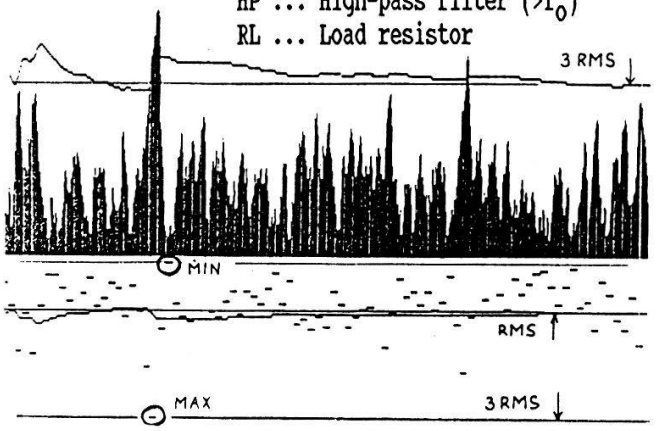

FIG.2 SAMPLE OF TREATED NOISE.

Noise summation generated by five independent RLC circuits (Q = 500). Two rare events are visible.

Power combiner network: Noise energy coming from noise generators R (Fig.1) and idlers RI is confined within a narrow band around f_o. Idlers serve for a matched load so that independence of noise generators might be guaranteed. Noise generated by idlers enters the network in the opposite direction, but do not reach the output. It is dissipated in noise generators.

Nonlinearity: A hypothesis is suggested: "Nonlinearity is not an inherent property of a system; it depends, besides on temperature, on magnitudes and bandwidth of incident signals at system ports." Superimposed signals from noise generators have a shape of a sine wave (f_o) with slowly changing magnitude (Fig.2). This wave enters a lumped delay line T and is dissipated in the idler at the utmost right end of the network. The nonlinearity N is placed in the middle of the line instead of one of line inductances. It is formed by a transformer (Fig.3), which consists of a pot core (1) at a temp. T_1 with an air gap (5) and a ferrite rod (2) at its Curie temp. T_{c1}. Such a system need not necessarily obey Bridgman's principle of detailed balancing, because thermal equilibrium cannot be reached in a finite time. If the wave magnitude exceeds considerably the RMS of the noise signal, the ferrite rod (2) turns to nonlinear and begins to work as a freq. converter (f_o to $3f_o$). A small part of energy at $3f_o$ will be transfered through the high-pass filter HP to the load RL. For magnitudes comparable with, or smaller than the RMS, this transfer does not happen. Delay line and HP impedances are chosen so that energy transfer at $3f_o$ from the load RL back to the power combiner network might not occur (Fig.1: Point A: Z=R @ f_o, Z=0 @ $3f_o$; Point B: Z=0 @ $3f_o$; Point C: Z goes to infinity @ f_o, Z=RL @ $3f_o$). These requirements seem to be realizable.

Conclusions: 1. By using pure reactances, noise energy can be redistributed so that rare events might survive a longer time. 2. Small number of degrees of freedom can be realized and the recurence time shortened. 3. Perhaps, a nonlinearity can be designed (ferrimagnetic material at temp. just below its T_c), which behaves in a nonlinear way even for signal magnitudes of thermal noise. 4. Response time of this nonlinearity can be made shorter than the noise generator autocorrelation function. 5. With matched power combiners, noise signals can be superimposed, while their independence remains guaranteed.

FIG.3 NONLINEARITY AT CURIE TEMPERATURE.

1 ... Pot core @ $T_1 < T_{c2}$ (Curie temperature T_{c2})
2 ... Ferrite rod @ T_{c1} (Curie temperature $T_{c1} < T_{c2}$)
3 ... Primary winding
4 ... Secondary winding
5 ... Air gap
6 ... Circulating fluid at temperature $T_1 < T_{c1}$
7 ... Circulating fluid at temperature $T_2 > T_{c1}$

$T_1 < T_{c1} < T_2 < T_{c2}$

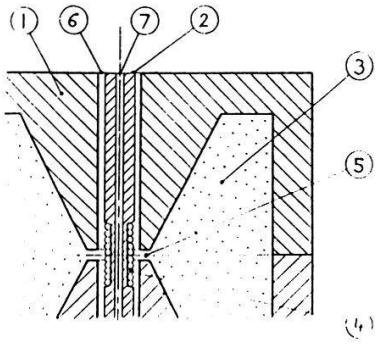

References: [1] S. Chandrasekhar, Rev. Mod. Phys. 15, 1-89 (1943)
[2] W.R. Bennett, Proc. IRE 44, 609-638 (1956)
[3] B.M. Oliver, Proc. IEEE 53, 436-454 (1965)

Zeros of Husimi functions for two-spin systems

Nicolas Regez, Stefan Weigert and Harry Thomas
Universität Basel, Institut für Physik, Klingelbergstraße 82, CH-4056 Basel

Pure quantum states of two-spin systems are shown to be uniquely determined by appropriate sets of zeros of their Husimi functions. For that purpose, reduced (analytic) quantum surfaces-of-section are defined. Analytic sections and the more familiar non-analytic sections are compared by numerical calculations.

The coherent-state representation of a pure one-spin state $|\psi\rangle$ is given by a complex polynomial: $\langle z|\psi\rangle = \sum_{m=-s}^{s} c_m z^{s+m}$, where s is the spin quantum-number and z is related to spherical coordinates ϑ and φ by a stereographic projection: $z = \tan\frac{\vartheta}{2}e^{i\varphi}$. The states $|m\rangle$ form the standard basis of the space $\mathbf{C}^{2s+1}$. Apart from norm and phase, the quantum state can be reconstructed if the $2s$ complex zeros of its Husimi function $W_\psi(z) = |\langle z|\psi\rangle|^2$ are known [1]. In the following, we generalize this method to systems consisting of two spins.

By projecting a pure two-spin state onto the coherent product-states $|z_1, z_2\rangle$ one obtains a complex polynomial of two variables z_1 and z_2, which may be rewritten as

$$\langle z_1, z_2|\psi\rangle = \sum_{m_2=-s}^{s}\sum_{m_1=-s}^{s} c_{m_1 m_2} z_1^{s+m_1} z_2^{s+m_2} = \sum_{m_2=-s}^{s} \xi_{m_2}(z_1) z_2^{s+m_2} . \qquad (1)$$

The quantities $|\xi_{m_2}(z_1)|^2$ represent the reduced or *analytic* quantum surfaces-of-section. The determination of their zeros for all possible values of m_2 [1] is *not* sufficient for the reconstruction of the ray $|\psi\rangle$ since they form a set of $(2s+1)$ $(2s)$-tupels of complex numbers only, whereas the definition of a ray in the space $\mathbf{C}^{2s+1} \otimes \mathbf{C}^{2s+1}$ requires the knowledge of $4s(s+1)$ complex numbers. Nevertheless, a partial reconstruction has been achieved because one can write $\psi(z_1, z_2; \{\alpha_{m_2}\}) = \sum_{m_2} \alpha_{m_2} \xi_{m_2}(z_1) z_2^{s+m_2}$, with known $\xi_{m_2}(z_1)$ and $(2s+1)$ yet undetermined complex numbers α_{m_2}, out of which only $2s$ are independent. To obtain the coefficients α_{m_2}, we write the wave function as $\psi(z_1, z_2) = \sum_{m_1} \eta_{m_1}(z_2) z_1^{s+m_1}$ and determine the function $\eta_{\widetilde{m}_1}(z_2)$ for one arbitrary value of $m_1 = \widetilde{m}_1$ from its zeros. Apart from a constant complex factor β, this function must coincide with the coefficient of $z_1^{s+\widetilde{m}_1}$ in $\psi(z_1, z_2; \{\alpha_{m_2}\})$:

$$\beta\, \eta_{\widetilde{m}_1}(z_2) = \frac{1}{(s+\widetilde{m}_1)!}\left(\frac{\partial}{\partial z_1}\right)^{s+\widetilde{m}_1} \psi(z_1, z_2; \{\alpha_{m_2}\})\bigg|_{z_1=0} . \qquad (2)$$

Both sides of equation (2) are polynomials in z_2, leading in the generic case to a sufficient number of implicit equations for the numbers α_{m_2}, and, *a fortiori*, to a unique ray $|\psi\rangle$. The case of N spins can be treated similarly.

In *non-analytic* quantum surfaces-of-section, ϑ_2 is fixed to a constant value Θ and φ_2 is calculated with the aid of the classical Hamiltonian by choosing a definite energy E_{cl}.

As an example, consider the family of two-spin models [2] described by the Hamiltonian $H_{\alpha\gamma} = -J\left\{(1+\gamma)\, S_{1x}S_{2x} + (1-\gamma)\, S_{1y}S_{2y} + \frac{1}{2}\alpha\left(S_{1x}^2 - S_{1y}^2 + S_{2x}^2 - S_{2y}^2\right)\right\}$. We have computed analytic and non-analytic sections of eigenstates of $H_{\alpha\gamma}$ for $s = 24$.

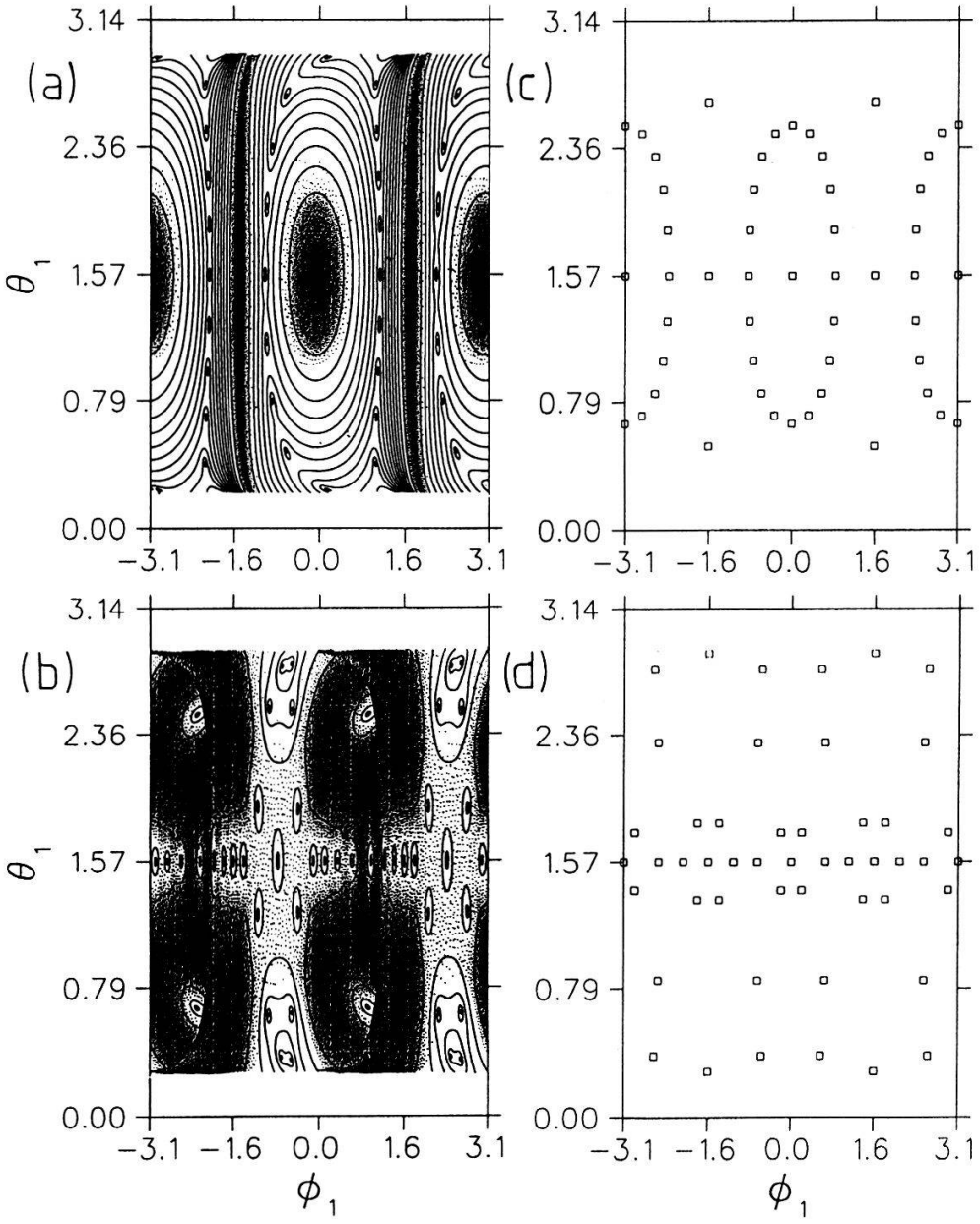

Figure.
Eigenstates of two-spin models $H_{\alpha\gamma}$. The zeros of the *non-analytic* sections (cut conditions: $\vartheta_2 = \frac{\pi}{2}$, $\dot{\vartheta}_2 > 0$) for (a) a classically integrable case ($\alpha = 0$, $\gamma = 0.5$) and (b) a classically non-integrable case ($\alpha = 0.7$, $\gamma = 0$) appear as dark blobs on a logarithmic scale. In (c) and (d), the zeros of the reduced or *analytic* sections for $m_2 = 0$ of the same two eigenstates are drawn.

The analytic quantum sections $|\xi_{m_2}(z_1)|^2$ for fixed m_2 and the corresponding non-analytic quantum sections are expected to coincide for high quantum number s. The zeros of both types of sections are seen to exhibit similar patterns.

However, in some cases there occur zeros of the analytic sections situated in high-density regions of the non-analytic sections (see figure (a) and (c) at $\varphi_1 = 0$, $\vartheta_1 = \frac{\pi}{2}$). This exceptional behaviour is possibly related to the fact that non-analytic sections are restricted to one traverse-direction through the classical energy surface, while the analytic sections pick up a contribution at each crossing of the energy surface along the path of integration [3].

This work has been supported by the Swiss National Science Foundation.

[1] P. Lebœuf: J. Phys. A**24**, 4575 (1991).

[2] N. Srivastava, C. Kaufman, G. Müller, R. Weber, H. Thomas: Z.Phys. B**70**, 251 (1988).

[3] P. Lebœuf, M. Saraceno: J. Phys. A**23**, 1745 (1990),
M. B. Cibils, Y. Cuche, P. Lebœuf, W. F. Wreszinski: Phys. Rev. A**46**, 4560 (1992).

PRIMARY PRUNED REGION FOR A 2D MAP

J. VOLLMER

Physics Institute, University of Basel, Klingelbergstr. 82, 4056 Basel, Switzerland

Symbolic dynamics and pruning are discussed analytically for a family of generalized Baker transformations. In contrast to numerical findings on similar maps (e. g. the Hénon map) we find more complex forms of the primary pruned region. In particular it need not be simply connected and need not have monotonic boundaries.

Generalized Baker transformations are frequently used to obtain insight into the behaviour of complex systems by explicit analytical discussion, while more complicated models only allow for numerical treatment [1]. In this spirit, the symbolic dynamics and grammar is discussed for a family of generalized Baker transformations

$$\mathcal{F}_{\eta,\xi}: \begin{pmatrix} x_{n+1} \\ y_{n+1} \end{pmatrix} = \begin{pmatrix} \eta\, x_n \\ \xi^{-1}\, y_n \end{pmatrix} + s_n \begin{pmatrix} 1-\eta \\ 1-\xi^{-1} \end{pmatrix} \tag{1}$$

where s_n takes the value 0 (1) when (x_n, y_n) lies below (above) the critical line $y_n = (1-m)/2 + m\,x_n$ with slope $m = -\eta(1-|\xi|)(1-|\eta|)^{-1}$. This discussion sheds new light on previous numerical work concerning a geometrical representation of the grammatical rules of symbolic dynamics [2].

By inspection one verifies that (1) is solved by $x_n = (1-|\eta|)\sum_{i=0}^{\infty}\eta^i\, s_{n-1-i}, y_n = (1-|\xi|)\sum_{i=0}^{\infty}\xi^i\, s_{n+i}$. As a consequence the areas above and below the critical line form a generating partition of a symbolic dynamics, and its grammar is given by the self-consistency conditions (SCC)

$$s_n = \Theta\left(s_n - \frac{1}{2}\frac{1-m}{1-\xi} + \sum_{i=1}^{\infty}(\eta^i\, s_{n-i} + \xi^i\, s_{n+i})\right) \tag{2}$$

that have to be fulfilled by a valid sequence $< s_{n+i} >_{i=-\infty}^{\infty}$ for any n . Geometrically this implies that the corresponding point (x_n, y_n) must always fall on that side of the partition line that is predicted by s_n. Due to the above representation of (x_n, y_n) by $< s_{n+i} >_{i=-\infty}^{\infty}$ the invariant set is contained in a 2D Cantor set with scaling η (ξ) along the x-axis (y-axis)

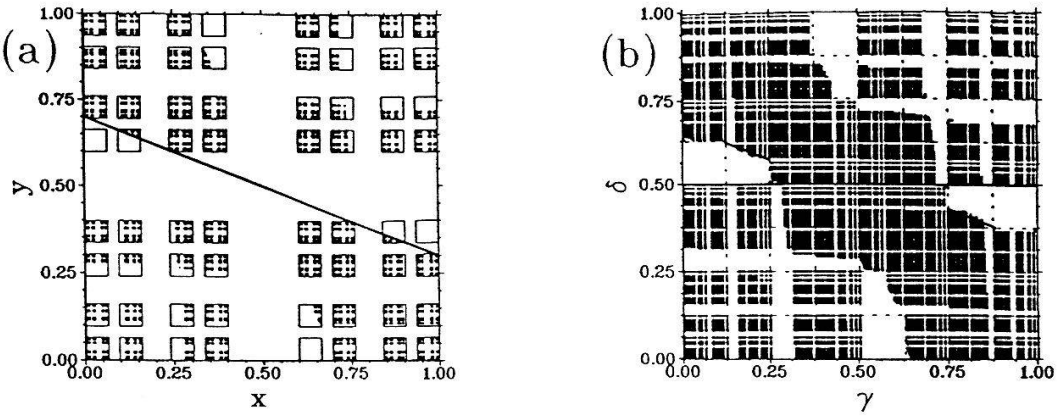

Figure 1: Invariant set in configuration plane (a) and symbol plane (b) of $\mathcal{F}$ at parameter values $\eta = \xi = .4$.

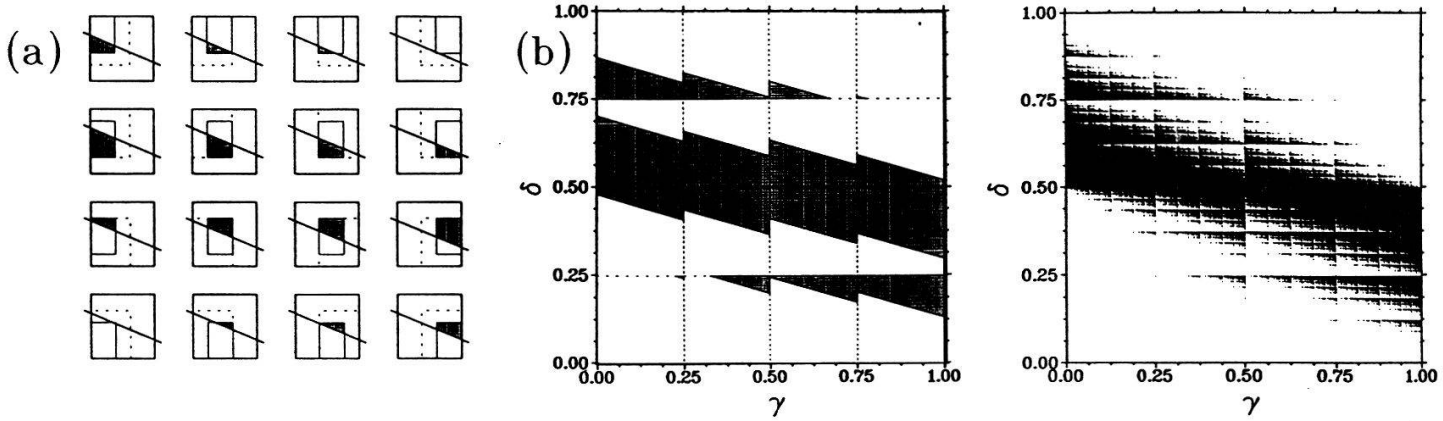

Figure 2: Construction of the primary pruned region of $\mathcal{F}$ at parameter values $\eta = .625$ and $\xi = .75$. (a) 2^{nd} order boxes and the corresponding forbidden area (hatched) in configuration space. (b) The primary pruned region as obtained by piecing together the information of (a) (left) and by the same construction for 9^{th} order boxes (right).

provided that η and ξ are smaller than .5. In that case the SCC can be interpreted geometrically as an absorbing area and all points that enter it under forward or backward iteration with (1) are forbidden (Fig 1a).

For the discussion of the allowed binary sequences it is more convenient to avoid the fractal structure of the invariant set and interpret $< s_{n+i} >_{i=-\infty}^{\infty}$ as two binary numbers $\gamma = .s_{n-1}\, s_{n-2}\, s_{n-3}\, s_{n-4} \ldots$ and $\delta = .s_n\, s_{n+1}\, s_{n+2}\, s_{n+3} \ldots$, In this representation missing points correspond to forbidden symbol sequences (cf. Fig 1b and [2]) and all points of the unit square are taken when no sequences are forbidden. The γ-δ-plane is denoted as *symbol plane* in the literature. It has been conjectured that in general the absorbing area, called *primary pruned region* (PPR), can be chosen to be simply connected and have smooth monotonic boundaries in this representation [2]. This is indeed what we also observe in Fig 1 and for any other parameter values as long as η and ξ are smaller than .5.

For $\xi > .5$, however, the decomposition into symbols is no longer unique and boxes of the Cantor set start to overlap. These boxes still give bounds to the position of points with a given truncated symbol sequence $< s_i >_{i=-k}^{k-1}$. A k^{th} order approximation to the PPR may be obtained by geometrically testing the SCC for boxes to k^{th} order and piecing this information together in the symbol plane as shown in Fig 2. Due to overlap of boxes, islands appear with boundaries that split again into chains of boundaries under finer resolution (Fig 2b). The author strongly expects that the primary pruned region takes a fractal structure in the limit $\xi \nearrow 1$. He has checked that it is not possible to reduce this complicated PPR into a simply bounded area by either dropping points that violate the SCC another time or by adding forbidden points in between the islands. This implies that looking for the simplest form of the PPR, as it has been done in previous numerical work [2], need not be the best strategy for understanding the symbolic dynamics of a dynamical system.

The author would like to thank W. Breymann, M. Eisele, P. Grassberger and T. Tél for stimulating discussions and valuable remarks, and the Swiss National Science Foundation for financial support.

References

[1] e. g. J. Guckenheimer, P. Holmes: *Nonlinear Oscillations, Dynamical Systems, and Bifurcations of Vector Fields* (Springer 1983), Chap. 5.7 and 5.8.

[2] Cvitanović, Physica D **51**, 138 (1991); d'Alessandro, e. a. J. Phys. A **23**, 5285 (1990).

Squeezing Energy Locally out of the Vacuum

Stefan Weigert

Universität Basel, Institut für Physik, Klingelbergstraße 82, CH-4056 Basel

A one-dimensional box partly filled with a dielectric medium, $\epsilon > 1$, is considered as a model of a laser. The requirement that initially the electromagnetic energy be localized as much as possible in a finite region of the box is satisfied if each normal mode of the field is prepared in a squeezed state. In these states the expectation value of the energy density integrated over a specific volume is *smaller* than compared to its value in the quantum-mechanical vacuum. In principle, this result can be used to increase the force acting on a perfectly conducting plate in a Casimir-type situation.

A one-dimensional box of length $L = \lambda + \Lambda$ is considered as a model of a laser [1]. Region I: $-\lambda \leq x < 0$, is filled with a dielectric medium, $\epsilon > 1$, representing the lasing cavity, and region II: $0 < x \leq \Lambda$, stands for the empty "universe" with $\epsilon = 1$. The discontinuity in ϵ at $x = 0$ acts as a semitransparent mirror for electromagnetic radiation. The solutions $v_k(x)$ of the wave equation ($c = 1$) for the electric field,

$$\frac{d^2 v_k(x)}{dx^2} + \epsilon(x)\omega_k^2 v_k(x) = 0\,, \qquad k = 1, 2, \ldots, \tag{1}$$

vanish at the boundaries, $v_k(-\lambda) = v_k(\Lambda) = 0$, and constitute a complete set of orthonormal functions on the interval $-\lambda \leq x \leq \Lambda$

$$\int_{-\lambda}^{\Lambda} dx\, v_k(x) v_{k'}(x) = \delta_{kk'}\,, \quad \text{and} \quad \sum_{k=1}^{\infty} v_k(x) v_k(y) = \delta(x-y)\,. \tag{2}$$

In order to study the dissipative properties of the cavity, one looks for appropriate states which initially localize the energy of the field as much as possible in region I. Classically, all fields nonzero in region I and vanishing in region II serve this purpose. A natural quantum-mechanical formulation of this condition with as yet undetermined states $|\phi\rangle$ reads

$$\langle\phi|\,\widehat{W}_I\,|\phi\rangle > \min \quad \text{and} \quad \langle\phi|\,\widehat{W}_{II}\,|\phi\rangle = \min\,, \tag{3}$$

where the electromagnetic energy $\widehat{W}_I$ is given by integrating the operator of the energy density $\widehat{w}(x) = (\epsilon(x)\widehat{E}^2(x) + \widehat{H}^2(x))/2$ over region I: $\widehat{W}_I = \int_I dx\, \widehat{w}(x)$. Let the operators a_k and $a_k^\dagger$ be the annihilation and creation operators of photons with frequency ω_k, fulfilling $[a_k, a_\ell^\dagger] = \delta_{k\ell}$. Then the field operator $\widehat{E}$ can be expressed in terms of the eigenmodes $v_k(x)$ of the box as $\widehat{E}(x,t) = \sum_{k=1}^{\infty} v_k(x)\widehat{e}_k(t)$, where $\widehat{e}_k(t) = i\sqrt{\omega_k/2}(a_k \exp(-i\omega_k t) - a_k^\dagger \exp(i\omega_k t))$; similarly, $\widehat{H}(x,t) = \sum_{k=1}^{\infty} \partial_x v_k(x)\widehat{h}_k(t)$. In this way the Hamiltonian of the system is seen to be equivalent to a collection of uncoupled harmonic oscillators with frequencies ω_k. At time $t = 0$, the second condition in Eq. (3) can be written as

$$\frac{1}{2}\int_{II} dx \left(\epsilon(x)\langle\widehat{E}(x)\rangle^2 + \langle\widehat{H}(x)\rangle^2\right) + \sum_{k=1}^{\infty}\left(V_k(\Delta\widehat{e}_k)^2 + \overline{V}_k(\Delta\widehat{h}_k)^2\right) = \min\,, \tag{4}$$

where $(\Delta\widehat{e}_k)^2 \equiv \langle\widehat{e}_k^2 - \langle\widehat{e}_k\rangle^2\rangle$, etc., with the positive real numbers $V_k = \int_{II} dx\, \epsilon(x) v_k^2(x)/2\omega_k$ and $\overline{V}_k = \int_{II} dx\, (\partial_x v_k)^2(x)/2\omega_k$, and all expectation values are taken with respect to the state $|\phi\rangle$. The sum in Eq. (4) takes on its minimal value if each of the positive terms is as small as possible; however, the commutation relation $[\widehat{e}_k, \widehat{h}_k] = i$ implies the constraint $(\Delta\widehat{e}_k)^2(\Delta\widehat{h}_k)^2 \geq 1/4$. It follows that $\langle\widehat{E}(x)\rangle = \langle\widehat{H}(x)\rangle = 0$ in region II and

$$2(\Delta\widehat{h}_k)^2 = \mu_k = 1/2(\Delta\widehat{e}_k)^2 \quad \rightarrow \quad (\Delta\widehat{e}_k)^2(\Delta\widehat{h}_k)^2 = 1/4\,, \tag{5}$$

where $\mu_k = (V_k/\overline{V}_k)^{1/2}$. Consequently, each field mode is required to be in a *minimum uncertainty state,* the most general form of which is a *squeezed state* $|\phi_k(\Lambda)\rangle \equiv |\{r_k, \beta\}\rangle$, *i.e.*, an eigenfunction of the operator $\widehat{D} = a_k \cosh r_k + a_k^\dagger \sinh r_k$ with eigenvalue $\beta_k = (\langle\widehat{e}_k\rangle - i\mu_k\langle\widehat{h}_k\rangle)/\sqrt{2\mu_k}$, and the squeezing parameter $r_k = -\ln\sqrt{\omega_k\mu_k}$ [2]. Let $|\phi(\Lambda)\rangle = \otimes_{n=1}^{\infty} |\phi_n(\Lambda)\rangle$ denote the state of the field in which each mode is squeezed. Then one finds

$$\langle\phi(\Lambda)|\widehat{W}_{II}|\phi(\Lambda)\rangle = \sum_{k=1}^{\infty}\omega_k(V_k\overline{V}_k)^{1/2} \leq \frac{1}{2}\sum_{k=1}^{\infty}(\omega_k^2 V_k + \overline{V}_k) = \langle 0|\widehat{W}_{II}|0\rangle\,, \tag{6}$$

showing that the expectation value of the energy contained in region I is *less* than its value in the quantum-mechanical ground state, the vacuum state $|0\rangle$. For the total energy, $\widehat{W} = \widehat{W}_I + \widehat{W}_{II}$, one still has $\langle\phi(\Lambda)|\widehat{W}|\phi(\Lambda)\rangle > \langle 0|\widehat{W}|0\rangle$, as is required on general grounds. In other words, the zero-point energy has been partially squeezed out of region II and into region I by the appropriate excitation of quantum states. This phenomenon which does not have a classical counterpart can be used to modify the Casimir force [3] on two parallel, perfectly conducting plates in the vacuum with distance L. This attractive force can be understood to arise from the difference in the zero-point energies associated with the discrete spectrum of the field between the plates and the continuous spectrum in the outer regions; after renormalization on finds a finite difference $W_C = \sum_{k=1}^{\infty}\omega_k/2 - \int_0^{\infty} d\omega\,\omega/2 \sim -L^{-d}$, so that $F_C = -\partial W_C/\partial L \sim -L^{-(d+1)}$, where d is the number of spatial dimensions. In the above model but with $\epsilon(x) = 1$ everywhere and the parameter $\eta \equiv \lambda/L \ll 1$, the contribution $\Delta W_{II}^k = -\sin^2(2\pi k\eta)/16\pi kL$ of a single squeezed mode with index k leads to a decrease of the Casimir energy in region II: $W_{II,C}^k = W_{II,C} + \Delta W_{II,C}^k < W_{II,C}$. To first order in η one finds an *increased* Casimir force acting on the plate at the right end

$$F_{II,C}^k \equiv \frac{\partial\Delta W_{II,C}^k}{\partial\Lambda} \sim -(1 + \gamma_k\eta)L^{-2}\,, \tag{7}$$

with a constant γ_k being positive if $k < 1/4\eta$. Since squeezed states are not eigenstates of the Hamiltonian, the strength of $F_{II,C}^k$ will vary in time.

References

[1] This model has been introduced in: St. Weigert, Diplomarbeit RWTH Aachen (1986), work performed under the auspices of Prof. N. G. van Kampen.

[2] D. Stoler: Phys. Rev. D **1** (1970) 3217

[3] G. Plunien, B. Müller and W. Greiner: Phys. Rep. 134 (1986) 87